Geophysical Journal International

Geophys. J. Int. (2012) **189,** 761–781 doi: 10.1111/j.1365-246X.2012.05395.x

Core surface magnetic field evolution 2000–2010

C. C. Finlay,[1,2] A. Jackson,[1] N. Gillet[3] and N. Olsen[2]

[1] *Institute of Geophysics, Sonneggstrasse* 5, *ETH Zurich, Zurich,* CH-8092, *Switzerland. E-mail: cfinlay@space.dtu.dk*
[2] *DTU Space, Juliane Maries Vej* 30, 2100 *Copenhagen, Denmark*
[3] *ISTerre, Université de Grenoble* 1, *CNRS,* F-38041, *Grenoble, France*

Accepted 2012 January 27. Received 2012 January 27; in original form 2011 September 30

SUMMARY

We present new dedicated core surface field models spanning the decade from 2000.0 to 2010.0. These models, called *gufm-sat*, are based on CHAMP, Ørsted and SAC-C satellite observations along with annual differences of processed observatory monthly means. A spatial parametrization of spherical harmonics up to degree and order 24 and a temporal parametrization of sixth-order B-splines with 0.25 yr knot spacing is employed. Models were constructed by minimizing an absolute deviation measure of misfit along with measures of spatial and temporal complexity at the core surface. We investigate traditional quadratic or maximum entropy regularization in space, and second or third time derivative regularization in time. Entropy regularization allows the construction of models with approximately constant spectral slope at the core surface, avoiding both the divergence characteristic of the crustal field and the unrealistic rapid decay typical of quadratic regularization at degrees above 12. We describe in detail aspects of the models that are relevant to core dynamics. Secular variation and secular acceleration are found to be of lower amplitude under the Pacific hemisphere where the core field is weaker. Rapid field evolution is observed under the eastern Indian Ocean associated with the growth and drift of an intense low latitude flux patch. We also find that the present axial dipole decay arises from a combination of subtle changes in the southern hemisphere field morphology.

Key words: Rapid time variations; Satellite magnetics.

1 INTRODUCTION

The decade from 2000.0 to 2010.0 was the first for which Earth's magnetic field was continuously monitored from space by satellites, as well as by a ground network of observatories. This massive monitoring effort has yielded high quality data sets that can be used to study the evolution of Earth's magnetic field and its origin in the dynamics of the liquid metal outer core. The mechanisms controlling geomagnetic secular variation (SV) are not yet fully understood; detailed, reliable, observations of the core field and its time derivatives have an important role to play in the elucidation of these processes. Geomagnetic observations guide hypotheses, and also provide the crucial empirical tests for models of core magnetohydrodynamics.

Discrete geomagnetic observations (e.g. the northward X, eastward Y and radially inwards Z, vector components or scalar measurements of the field intensity F—see for example, Hulot *et al.* 2007) can be combined into 'field models' that are continuous functions of space and time (Bloxham & Jackson 1992; Jackson *et al.* 2000; Sabaka *et al.* 2004; Gillet *et al.* 2010). These encapsulate the information content related to the core field present in the observations. Models of the internal part of the main geomagnetic field (hereafter MF) are usually parametrized in terms of the internal, spherical harmonic based, series solutions to Laplace's equation. We follow this classical approach, neglecting electrical currents in the mantle, and assuming that such a model is valid from the surface of the core up to satellite altitudes. We construct spherical harmonic models of the core field that are continuous in time, so they can be differentiated once to study instantaneous SV or twice to study instantaneous secular acceleration (SA) of the field, which provides additional insight into the mechanisms of field evolution (e.g. Holme *et al.* 2011). Here we use CHAMP, Ørsted and SAC-C satellite observations together with annual differences of observatory monthly means to construct models that span the interval from 2000.0 to 2010.0; further details of the observations including the processing steps performed to minimize the influence of unmodelled external fields are described in Section 2.

We refer to our new core field models by the name *gufm-sat*, followed by a qualification that indicates the choice of regularization norms. Such terminology is appropriate because our method is essentially similar to that employed in *gufm1* (Jackson *et al.* 2000), with the core field parametrized in terms of a spline temporal representation of spherical harmonics, and involves minimizing both the misfit to observations and norms measuring the spatial and temporal complexity of the core surface field. The *gufm-sat* models are also an important intermediate step towards extending *gufm1* to 2010.

The *gufm-sat-E3* model with entropy regularization in space is essentially a time-dependent extension of the single epoch model for 2000.0 presented by Jackson (2003). A more detailed description of the modelling method is found in Section 3.

A number of other time-dependent field models already exist that span all or parts of the interval from 2000.0 to 2010.0. However, these models primarily focus on producing accurate models of the geomagnetic field at Earth's surface for operational purposes, such as contributing to the International Geomagnetic Reference Field (IGRF). They include the CHAOS series of models (Olsen *et al.* 2006, 2009, 2010) and the GRIMM series of models (Lesur *et al.* 2008, 2010). Both these series of models also use a B-spline temporal representation and impose similar temporal regularization, and both have proven useful for studying the core field. In contrast to our approach, these models simultaneously solve for not only the core field, but also for the crustal field and the large scale external field. In Section 4, we compare our *gufm-sat* models to recently published CHAOS and GRIMM models. As well as spline based models, there are also a number of models of the recent field that adopt a simpler (piecewise) Taylor series temporal representation; these include the POMME series (Maus *et al.* 2006, 2010), the models developed at the British Geological Survey (Thomson & Lesur 2007; Hamilton *et al.* 2010) and those constructed by Thébault *et al.* (2010).

Given the plethora of existing field models, is there a need for new models for the past decade? We argue that there is a role to be played by dedicated models of the core field, constructed using a relatively small number of degrees of freedom, specifically designed for the study of core dynamics. For example, these may be useful as inputs to core flow inversions (e.g. Holme 2007) or in comparisons with geodynamo simulation output (e.g. Fournier *et al.* 2011). The *gufm-sat* models are close in spirit to the CHAOS and GRIMM models; the major difference is that the *gufm-sat* models focus entirely on the core field, employ spatial regularization at the core surface and that estimates of the crustal and external fields are subtracted from the data prior to modelling. The resulting differences in the spherical harmonic spectra of the *gufm-sat* models compared to those of the CHAOS and GRIMM models are described in Section 4. Note that compared to the GRIMM model we use vector data at mid and low latitudes, but only scalar data at higher latitudes; we also use data from the satellites Ørsted and SAC-C so we can study the whole decade from 2000 to 2010. Compared to the CHAOS models we use only a relatively small subset of the available observations, to obtain data coverage that is as homogeneous as possible in space and time. This means we also typically have lower spatial density of data, but this is acceptable for our purposes because we seek to model only the core field and not the small scale crustal field. In terms of the correction of data for external field effects prior to modelling, our approach is somewhat similar to that taken in the POMME models. However, unlike the POMME models, we use a robust (L_1-norm) measure of misfit (Walker & Jackson 2000) to help us cope with the remaining non-Gaussian noise from unmodelled external field fluctuations.

In Section 4, we present three new core surface field models: (i) *gufm-sat-Q2* which is constructed using quadratic spatial regularization and second time derivative temporal regularization; (ii) *gufm-sat-Q3* which involves the same spatial regularization but has third time derivative temporal regularization; (iii) *gufm-sat-E3* which involves entropy regularization in space and third time derivative temporal regularization. Further details concerning the construction and properties of the models can be found in Sections 3 and 4. These three models, which fit the data to a very similar level in a global sense, are presented to illustrate the flexibility available when modelling core field evolution, depending on the modelling strategy adopted. Nonetheless, we finally prefer models *gufm-sat-Q3* and *gufm-sat-E3*, concluding these are superior because *gufm-sat-Q2* contains temporal variations that are not required to satisfactorily fit the observations. In Section 5, we highlight findings that are robust across the *gufm-sat* models with important implications for core dynamics and the mechanisms underlying SV. Noteworthy features include the asymmetry between the Pacific (approximately 140° east to 100° west) and Atlantic (the remaining 100° west to 140° east) hemispheres, the evolution of the series of intense field features north and south of the geomagnetic equator under the Atlantic hemisphere (hereafter referred to as the low latitude 'wavetrains'), and the continuing decay of the geomagnetic axial dipole.

2 OBSERVATIONS

This study is based on both satellite observations and measurements made at the global network of geomagnetic ground observatories. Because we estimate only the core field, the data must be carefully selected and processed prior to inversion. The aim was to obtain a high quality data set primarily measuring the core field, with sufficient spatial coverage to resolve core field variations and with temporal resolution sufficient to capture subannual variations.

2.1 Satellite data

The satellite data employed are a subset of that compiled by Olsen *et al.* (2010) for production of the *CHAOS-3* field model. We use the part of this data set that comprises three component vector field data from the Ørsted (between 2000 January and 2004 December) and CHAMP (between 2001 January and 2009 December) satellites, as well as scalar intensity measurements from the Ørsted (between 2000 January and 2009 December), CHAMP (between 2000 August and 2009 December) and SAC-C (between 2001 January and 2004 December) satellites. Selection criteria designed to highlight geomagnetically quiet conditions were employed, the same as those used for the *CHAOS* (Olsen *et al.* 2006) and *CHAOS-2* (Olsen *et al.* 2009) models. In terms of the storm time index D_{st} and the global geomagnetic activity index *Kp* (Mayaud 1980) it was required that $|dD_{st}/dt| < 2\text{nT hr}^{-1}$, that $Kp \leq 2o$ for non-polar latitudes, and that the merging electric field at the magnetopause be less than $0.8\,\text{mVm}^{-1}$. In addition, vector data are only used equatorward of 60° geomagnetic latitude to minimize the influence of field-aligned currents, CHAMP non-polar data were used only after local midnight to avoid diamagnetic plasma effects, and only data from dark regions (sun 10° below horizon) were accepted. Further details concerning these criteria are given in Olsen *et al.* (2006). The vector data used for our modelling were rotated from the measurement frame of the instrument to a geocentric coordinate system using the Euler angles coestimated during the derivation of the *CHAOS-3* field model. For the scalar data from CHAMP and Ørsted we performed an additional calibration step compared to the data used by Olsen *et al.* (2010), designed to mitigate a known minor incompatibility between these data sets (e.g. Thébault *et al.* 2010). This involved multiplying by a factor $(1+\epsilon)$ where $\epsilon = 1.0 \times 10^{-5}$ for CHAMP scalar data and -3.5×10^{-5} for Ørsted scalar data; no correction was applied the the SAC-C scalar data.

Rather than use the entire data set of Olsen *et al.* (2010), we choose to resample it to produce a data set with a more homogeneous spatial and temporal coverage. We constructed an

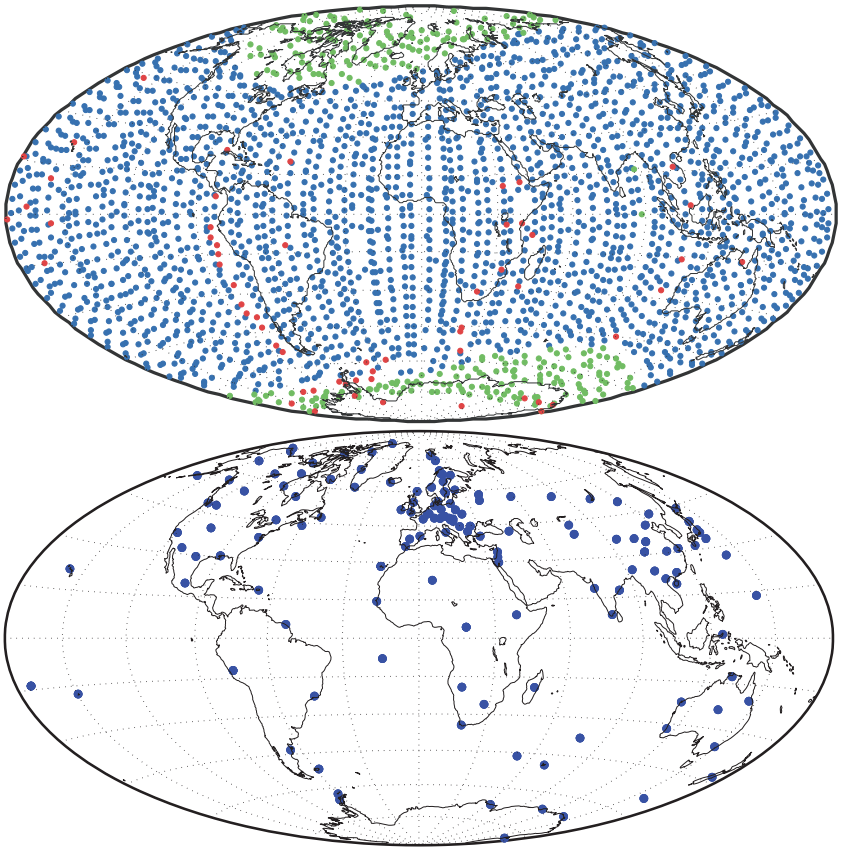

Figure 1. Distribution of satellite data as a function of latitude and longitude (top panel) used for the 3 months 2008 January to March. Blue is a CHAMP vector measurement, green is a CHAMP scalar measurement, red denotes an Ørsted scalar measurement. The bottom plot shows the locations of magnetic observatories at Earth's surface used in this study.

approximately equal area grid consisting of 72 cells uniformly spaced in longitude by 36 cells uniformly spaced in cosine of latitude. In each cell, one observation (either a three component vector observation or a scalar observation) was selected every 0.25 yr whenever possible. CHAMP vector data were selected when possible, then Ørsted vector data, then CHAMP scalar intensity data, then Ørsted or SAC-C intensity data. As an example, the latitude–longitude distribution of satellite observations for 2008 January to March is shown in the top panel of Fig. 1. The majority of the data are from the CHAMP satellite, with vector data selected outside the polar regions and scalar data selected within the polar regions. A small number of Ørsted data was used to fill gaps in the CHAMP coverage, but note that the latter observations occur at a higher altitude. Only a small number of data are located around the southern pole because it is mostly daytime in this region during this time interval. We stress that because we are concerned only with estimation of the core surface field (and not the crustal field), a very high density of observations is not necessary. Each satellite observation provides information on a weighted average of the core surface field (Gubbins & Roberts 1983) and not just on the field directly beneath. In Fig. 2 we present the number of observations used as a function of time. There are on the order of 2500 observations used in each 0.25 yr interval, which is sufficient for our purposes.

Our modelling procedure (Section 3) is focused on core field estimation, and does not explicitly model either the crustal field or external fields. Because both these sources can be resolved by the satellite data we employ, it is not sufficient to simply treat them as random noise. Instead we subtract from our data set the predictions

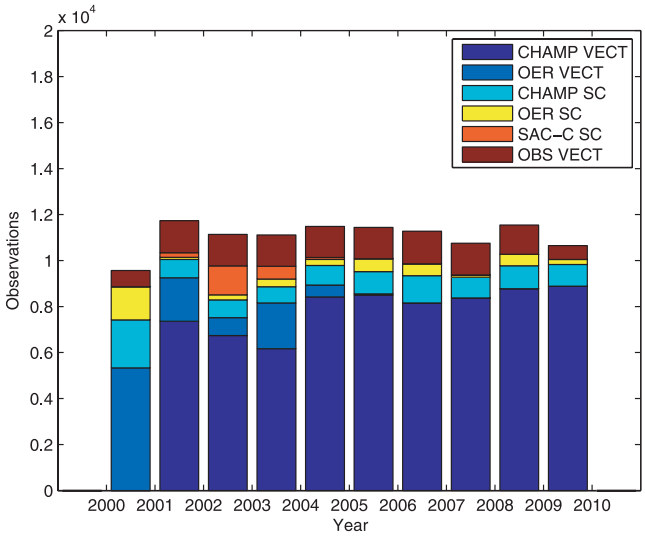

Figure 2. Temporal distribution of data from satellites and annual differences of observatory monthly means used in this study. Three component vector observations are counted as a single observation. Colours represent different data sources. Note that annual differences of observatory monthly means are represented here by their central time, hence the first and last bars contain only half as many data, because only central times from 2000.5 to 2001.0 and 2009.0 to 2009.5 are possible with monthly mean data between 2000.0 and 2010.0.

of a pre-existing model of the known part of the global crustal field [we choose to use the model *STT-CRUST-E* of Stockmann *et al.* (2009)] and the predictions of a large scale magnetospheric field model. For the latter we use the *CHAOS-3* external field model of Olsen *et al.* (2010), which is described in detail by Olsen *et al.* (2006), and takes into account variations of large scale current sources in the near magnetosphere (e.g. the ring currrent) and in the far magnetosphere (e.g. tail currents) as well as the most basic effects of induced fields in a 1-D, electrically conducting upper mantle. Although this procedure is undoubtedly imperfect, it is preferable to ignoring both the crustal field and the external field, and it allows us to use fewer model parameters in our inversions compared to studies that simultaneously invert for all sources. The largest static corrections due to the crustal field were made above strong continental anomalies, for example, above central Africa, northeastern Europe, eastern north America and western Australia; investigation of other crustal field models showed the choice of crustal model had little influence on the resulting core field models. For example, for the Z component vector data, the range of crustal corrections applied was -17.6–26.9 nT with an rms amplitude of 6.1 nT and a mean value of -0.2 nT. Predictions of the external field model usually resulted in corrections of amplitude less than 20 nT. It should however be borne in mind that no account was taken of fields due to ionospheric current sources, though these are expected to be small due to the selection of data from non-sunlit regions.

An important ingredient in the inverse problem described in Section 3 is the covariance matrix for the data. It is unfortunately very difficult to obtain rigorous *a priori* error estimates for satellite magnetic observations. The error budget must include measurement errors (e.g. due to errors in attitude determination) but also errors due to unmodelled fields, for example, the large scale crustal field that has not been deterministically removed, remaining unmodelled fields of magnetospheric origin, and also fields due to ionospheric currents (particularly field aligned currents, the auroral electrojet and polar cap currents that are significant at geomagnetic latitudes of 55° and higher). Residuals from previous field models show a clear increase towards auroral geomagnetic latitudes (Olsen 2002); for this reason we use an error budget that depends on geomagnetic latitude. Furthermore, different error budgets are used for the CHAMP and Ørsted/SAC-C satellites, due to their different altitudes (the influence of ionospheric currents and remaining crustal field is expected to be larger for CHAMP due to its lower altitude). For CHAMP scalar data, an error estimate σ_B of 3.0 nT is allocated for geomagnetic latitudes below 55° while a larger estimate of 10.0 nT is allocated for geomagnetic latitudes above 65°. For Ørsted/SAC-C scalar data an error estimate σ_B of 3.5 nT is allocated for geomagnetic latitudes below 55° while 8.5 nT is allocated for geomagnetic latitudes above 65°. A cosine taper function is used to gradually adjust the error estimates in the 10° between the 'low' and 'high' geomagnetic latitude regions. In addition to the scalar field errors, we take into account anisotropy of vector field errors in the reference frame of the magnetometer (Holme & Bloxham 1995; Holme 2000; Olsen 2002). For CHAMP vector data we set the angular errors $\psi = \chi = 10$ arc seconds (see Olsen (2002) for a definition of these angles) when both star cameras are operating and increase χ to 40 arc seconds when only one camera is operating. For Ørsted vector data we set $\psi = 10$ arc seconds but set $\chi = 40$ arc seconds after 2000 January 22 and to 60 arc minutes before this date. The error estimates adopted here are rather conservative, other workers may prefer to fit the data more closely. Our philosophy is try to use cautious error estimates in an attempt to avoid mapping spurious structure, for example, due to the crustal field, into the core field.

2.2 Observatory monthly means

In addition to satellite data, we also make use of measurements carried out at an international network of ground magnetic observatories. We use measurements from 135 observatories operating between 2000.0 to 2010.0. The locations of these observatories are shown in the bottom panel of Fig. 1. Although ground observatories lack the true global coverage of the satellite data, they provide high quality information on temporal changes from fixed locations at Earth's surface. Because observatory measurements are subject to crustal fields that change very little over 10 yr (Thébault *et al.* 2009), and because they are located below the ionosphere, they are an important complement to satellite data, placing very useful constraints on local SV and SA.

Because our focus is on modelling the core field, prior to using the observatory data we carried out processing designed to remove as much of the external and short period induced fields as possible. The basic underlying data were observatory hourly mean values obtained from the World Data Centre for Geomagnetism, Edinburgh. Data were selected from all local times. From these we subtracted the fields locally predicted by the CHAOS-3 external field model (Olsen *et al.* 2010). Because we use all local times it was also important to subtract a CM4 (Sabaka *et al.* 2004) type model of the fields of ionospheric origin and their corresponding Earth-induced counterpart. From these revised hourly means we then computed 'robust' monthly means using an iterative reweighting procedure based on an assumed Huber error distribution (Hogg 1979; Constable 1988; Huber 1996; Olsen 2002). This technique is known to produce estimates that are less affected by non-Gaussian outliers that can be present for example due to the non-random nature of the various non-core field sources. Finally the monthly means were checked manually, obvious base-line shifts corrected and gross outliers rejected. An earlier version of these 'revised' monthly means suitable for core field modelling was previously reported by Olsen *et al.* (2010); the present scheme differs in that for the earlier study time changes of the magnetospheric field were parametrized by $D_{st}(t)$, while here the full CHAOS-3 external field model, which accounts for baseline shifts in $D_{st}(t)$, is used.

To obtain error estimates for these 'revised' monthly means, we used the technique of generalized cross-validation or GCV (Green & Silverman 1994) to fit a cubic spline model to each component (X, Y or Z) at each observatory. The smoothness of the spline model is determined by the criteria to minimize the GCV score which approximates the ability of the spline model to predict data that are left out. The root mean square residual between the GCV spline model and the observations provides a useful estimate of the typical deviation between the component measurements and the underlying, smoothly varying, core field signal. The resulting error estimates are independent of time, but do vary with location and by component. During the field modelling, to desensitize the data to the crustal field and to emphasize time variations, we consider annual differences of the monthly means. This removes both the approximately stationary crustal field and annual (seasonal) variations due to remaining unmodelled external and concommitant induced fields. Error estimates for the annual differences of monthly means are finally obtained by a combination of the errors at the two times which are differenced to produce the SV estimate. We have however

not considered the correlation between errors in different field components at a given observatory described by Wardinski & Holme (2006, 2011).

3 CORE FIELD MODELLING METHODOLOGY

3.1 The forward problem

We seek a model capable of explaining these satellite and observatory data in terms of a magnetic field originating in the Earth's core. Because the Earth's mantle is a much poorer electrical conductor than the core (e.g. Kuvshinov & Olsen 2006; Medin *et al.* 2007; Velímský 2010), we neglect the weak electrical currents flowing in the mantle. Furthermore, any signature of the magnetized crust that has not been removed by the data processing is treated as unmodelled noise. Under these assumptions, the magnetic field in the region outside the core may be expressed as the gradient of a scalar potential V, which may be written as the following sum of spherical harmonics at a specified radius r

$$V(r,\theta,\phi,t) = a\sum_{l=1}^{L}\sum_{m=-l}^{l}\left(\frac{a}{r}\right)^{l+1} g_l^m(t)Y_l^m(\theta,\phi), \tag{1}$$

where θ is the geocentric colatitude, ϕ is longitude and $Y_l^m(\theta,\phi)$ are Schmidt quasi-normalized spherical harmonics of degree l and order m where $m \geq 0$ denotes the $\cos m\phi$ components and $m < 0$ denotes the $\sin m\phi$ components. L is the truncation degree of the expansion, chosen to be 24 for all the *gufm-sat* models, and $a =$ 6371.2 km is Earth's spherical reference radius.

Since we wish to model the temporal evolution of the core field, we further expand the Gauss coefficients $g_l^m(t)$ using a sixth-order B-spline basis with

$$g_l^m(t) = \sum_{n}^{N_{spl}} g_l^{mn} M_n(t), \tag{2}$$

where $M_n(t) > 0$ if $t \in |t_n, t_{n+6}|$ and is zero otherwise. A total of 51 knot points were employed, with a uniform 0.25 yr spacing to span the interval from 2000.0. to 2010.0; since ten of these knots are located symmetrically either before 2000.0 or after 2010.0 we have $N_{spl} = 45$ and the resulting field model consists of 28 080 parameters. The relatively large number of knots ensures that the SA will not be influenced by the chosen knot spacing and only by the imposed regularization. Sixth-order splines were adopted because we wish to use and interpret the first and second time derivatives of the core field.

The magnetic field components, X, Y, Z and F at any location and time of interest can easily be determined from the magnetic potential V (e.g. Bloxham *et al.* 1989, p. 418), so predictions concerning observables can be obtained from a given set of field model coefficients. If geomagnetic field observations are listed in a vector $\mathbf{d}$, and the model coefficients g_l^{mn} in a vector $\mathbf{m}$, the geomagnetic forward problem may be written in matrix form as

$$\mathbf{d} = \mathbf{f}(\mathbf{m}) + \mathbf{e}, \tag{3}$$

where $\mathbf{f}$ is the non-linear functional mapping the model to the predicted observable and $\mathbf{e}$ is an error vector of the misfit between the model predictions and the observations.

3.2 The inverse problem

The inverse problem involves finding a model $\mathbf{m}$ that adequately describes the evolution of the magnetic field at the core surface, given the available observations. This problem unfortunately does not have a unique solution: many possible field models can fit the observations to within their estimated errors (e.g. Parker 1994). One strategy for circumventing this problem is to seek geomagnetic field models that are as simple as possible while adequately fitting the data (Whaler & Gubbins 1981; Shure *et al.* 1982; Gubbins 1983; Gubbins & Bloxham 1985). This approach is usually referred to as 'regularization' or 'damping' (Parker 1994; Gubbins 2004; Aster *et al.* 2005). The regularization method used here is an extension of that used previously to construct time-dependent core field models by Bloxham & Jackson (1992), Jackson *et al.* (2000) and Gillet *et al.* (2007).

In brief, we search for models that minimize an objective function $\Theta(\mathbf{m})$ of the form

$$\Theta(\mathbf{m}) = Q(\mathbf{m}) + R(\mathbf{m}), \tag{4}$$

where $Q(\mathbf{m})$ is a measure of the misfits $e_i(\mathbf{m}) = d_i - [f(\mathbf{m})]_i$ between the model predictions and the observations (with vector data rotated into a frame where their errors between components are uncorrelated), and $R(\mathbf{m})$ is a norm measuring both the spatial and temporal complexity of the core surface field. We choose $Q(\mathbf{m})$ to be an L_1 norm measuring the absolute deviation between the model and the observations divided by their *a priori* error estimates σ_i,

$$Q(\mathbf{m}) = \sum_{i=1}^{N}\frac{|e_i(\mathbf{m})|}{\sigma_i}, \tag{5}$$

where N is the total number of observations. The L_1 misfit measure is known to be superior to the standard least squares L_2 method in the presence of non-Gaussian noise, for example, if outliers are present (Claerbout & Muir 1973; Aster *et al.* 2005; Tarantola 2005). It has been found to perform well in geomagnetism, producing robust field models (e.g. Walker & Jackson 2000; Thomson & Lesur 2007; Lesur *et al.* 2008) even when there is significant noise due to unmodelled fluctuations in the magnetospheric and ionospheric fields. We follow Walker & Jackson (2000) and use an Iteratively Reweighted Least Squares—IRLS algorithm (Schlossmacher 1971; Farquharson & Oldenburg 1998; Constable 1988) that involves a relatively minor modification of standard least squares scheme. Further details of the implementation are given by Walker & Jackson (2000).

The regularization term comprises two components measuring respectively the spatial and temporal complexity of the model

$$R(\mathbf{m}) = \lambda_S R_S(\mathbf{m}) + \lambda_T R_T(\mathbf{m}). \tag{6}$$

The damping parameters λ_S and λ_T are used to control the relative importance of data fit and model complexity. The choice of $R_S(\mathbf{m})$ and $R_T(\mathbf{m})$ embodies the modeller's prior information concerning what constitutes a physically reasonable model. In this study, we explore two choices for the spatial norm. The first is the square of the radial component of the magnetic field integrated over the core surface and over time, a very simple quadratic function of the model parameters.

The second measure of spatial complexity explored is an information entropy norm (Gull & Daniell 1978; Gull & Skilling 1990; Sivia & Skilling 2006). It is motivated by a desire to build field models with maximum multiplicity (i.e. that can come about through the maximum arrangements of magnetic flux) whilst satisfying the observations. Entropy regularization is widely applied in

image retrieval problems that arise across many disciplines. It has been found to perform well with both noisy and incomplete data, allowing retrieval of images with high contrast, without introducing unnecessary structure (e.g. Gull & Skilling 1984). It has also been successfully utilized in geomagnetism (Jackson 2003; Jackson *et al.* 2007; Gillet *et al.* 2007; Stockmann *et al.* 2009). Our implementation is identical to that described by Gillet *et al.* (2007), readers are referred to this study for further details including a mathematical statement of the norms. An extra parameter, known as the default parameter, must be specified when using entropy regularization. Following Jackson (2003) and Jackson *et al.* (2007) we set this equal to 10 μT.

In addition to choosing a spatial norm, we must also specify a norm measuring the temporal complexity. Traditionally, when using a cubic spline basis to model historical observations, this norm was chosen to be the square of the second time derivative of the radial magnetic field, integrated over the core surface and over time. This choice can be shown to be optimal with fourth order or cubic B-splines (De Boor 2001). For comparison purposes, we construct some models using this norm. However, since we have high quality satellite data with very good temporal coverage, and are interested in interpreting the second time-derivative (the SA), in this study we employ a basis of sixth-order splines. In this case one should use the square of the third time derivative of the radial magnetic field integrated over the core surface and over time as the regularization norm,

$$R_T(\mathbf{m}) = \frac{1}{t_e - t_s} \int_{t_s}^{t_e} \int_{\mathrm{CMB}} \left(\frac{\partial^3 B_r}{\partial t^3} \right)^2 d\Omega \, dt$$

$$= \frac{4\pi}{t_e - t_s} \int_{t_s}^{t_e} \sum_{l=1}^{L} \left(\frac{a}{c} \right)^{2l+4} \frac{(l+1)^2}{2l+1} \sum_{m=-l}^{l} \left(\frac{\partial^3 g_l^m(t)}{\partial t^3} \right)^2 dt, \quad (7)$$

where c is the core radius (3480 km), t_s is the start time of the model (2000.0) and t_e is the end time (2010.0), and the integration over $d\Omega$ denotes integration over the core–mantle boundary (CMB). Since we do not directly penalize the second time derivative this choice has the advantage of allowing us to interpret the SA without worrying that its amplitude may be artificially suppressed. However, similar to previous authors (Olsen *et al.* 2010; Lesur *et al.* 2010), in this case we find it necessary to explicitly apply additional conditions at the model start and end points setting the second time derivative to zero (via a penalty term with pre-factor 100), otherwise we obtain excessive power in the SA at small length scales.

Once the data set, error estimates, spatial and temporal norms, tuning (damping and default) parameters and temporal end point conditions have been specified, we solve the resulting optimization problem of minimizing the objective function (4). The objective function is non-linear because we use an L_1 measure of misfit, and because we sometimes use an entropy norm. To solve this non-linear optimization problem we use a Newton type iteration scheme (e.g. Luenberger 1969; Tarantola 2005) as described in Gillet *et al.* (2007). Iteration is carried out until the spatial and temporal norms of the differences between models at successive iterations change by less than 0.5 per cent. The misfit has by this stage also converged to at least three significant figures. To reach this point we carried out between 15 and 30 iterations depending on the choice of norms and damping parameters. At each iteration normal equation matrices were built in parallel for subsets of data, each stored in QR form, then recombined as required for the optimization algorithm.

Results from three field models constructed using the above technique are reported in the following sections. We refer to the model constructed using quadratic regularization in space and second time derivative temporal regularization as *gufm-sat-Q2* while a similar model that uses a third time derivative temporal regularization is called *gufm-sat-Q3*. *gufm-sat-E3* was constructed using entropy regularization in space and third time derivative temporal regularization. The latter two models also have zero second time derivatives imposed at the model start and end points. A description of the global properties (norms and misfits) of these models can be found in Table 1.

4 RESULTS

4.1 Spherical harmonic spectra

Fig. 3 presents spherical harmonic spectra (*cf.* Lowes 1974), evaluated at the core surface, for the MF, SV and SA of models *gufm-sat-Q2*, *gufm-sat-Q3* and *gufm-sat-E3* in epoch 2005.0. The models *CHAOS-3* (Olsen *et al.* 2010) and *GRIMM-2* (Lesur *et al.* 2010) from other authors are also shown for comparison, along with degrees 15–24 of the crustal field model *STT-CRUST-E* (Stockmann *et al.* 2009) downward continued to the core surface. The *gufm-sat* models were spatially regularized at the core surface; this ensures that their MF spectra converges (the power drops by two orders of magnitude by degree 24) at this radius. In contrast, the MF spectra for models *GRIMM-2* and *CHAOS-3* do not converge at the core surface, but exhibit an upward trend reminiscent of the crustal field (see the orange line denoting *STT-CRUST-E*). The MF spectra for model *gufm-sat-E3* exhibits a slope that is approximately constant out to its truncation degree, while for models *gufm-sat-Q2* and *gufm-sat-Q3* the quadratic spatial regularization forces a more rapid and unphysical spectral decay. The ability to obtain spectral slopes that do not decay in an artificial manner is an important characteristic of entropy regularized field models (Jackson 2003; Jackson *et al.* 2007; Gillet *et al.* 2007). It is arguably more physically realistic than enforcing hard truncation at some degree, for example, at degree 13, which leads to ringing in physical space because the spectra has not sufficiently decayed (Whaler & Gubbins 1981), or than strong filtering of power at high degree, as occurs with quadratic regularization, resulting in artificial smoothing in physical space. Degrees 14 to 24 of the MF in our models are however strongly controlled by the choice of regularization and default parameters; these have been chosen to be compatible with expectations from dynamo models (Jackson 2003; Jackson *et al.* 2007). In a sense they represent only one possible realization compatible with the assumed prior knowledge that is consistent with the observations, so these degrees should be interpreted with care. It is important to emphasize that all the models of the MF compared here agree very well up to degree 10, thereafter the form of spatial regularization or the truncation choice becomes important. Models without spatial regularization at the core surface contain significantly more power in the MF for degrees above 11.

The SV spectra presented in Fig. 3 further demonstrates that all the models studied agree very well up to degree 10. The spatially regularized *gufm-sat* models possess SV spectra that decrease above degree 13, while the SV spectra of *CHAOS-3* and *GRIMM-2* continue to increase with spherical harmonic degree. We advise workers interested in accurate spectral properties of the SV only to use degrees up to 13. Considering the SA spectra, the acceleration power begins to monotonically decrease above degree 6

Table 1. Statistics of global norms and misfits (L_1 norm dispersion measure) for different *gufm-sat* field models. The norms reported are $N_{B_r} = \frac{1}{t_e - t_s}\int_{t_s}^{t_e}\int_{\rm CMB} B_r^2\, d\Omega\, dt$, $N_{\partial_t B_r} = \frac{1}{t_e - t_s}\int_{t_s}^{t_e}\int_{\rm CMB}(\partial B_r/\partial t)^2\, d\Omega\, dt$, $N_{\partial_t^2 B_r} = \frac{1}{t_e - t_s}\int_{t_s}^{t_e}\int_{\rm CMB}(\partial^2 B_r/\partial t^2)^2\, d\Omega\, dt$, and $N_{\partial_t^3 B_r} = \frac{1}{t_e - t_s}\int_{t_s}^{t_e}\int_{\rm CMB}(\partial^3 B_r/\partial t^3)^2\, d\Omega\, dt$. The *gufm-sat-Q* models with quadratic spatial regularization have $\lambda_S = 1.25 \times 10^7\,{\rm nT}^{-2}$, the *gufm-sat-E3* model involves entropy spatial regularization with $\lambda_s = 1.0 \times 10^6\,{\rm nT}^{-2}$ and the same default parameter of 10 μT as used by Jackson (2003). The second and and third time derivative regularized models have $\lambda_T = 8.0 \times 10^{-3}\,({\rm nT\,yr}^{-2})^{-2}$ and $\lambda_T = 1.0 \times 10^{-2}\,({\rm nT\,yr}^{-3})^{-2}$, respectively.

Model	N_{B_r}	$N_{\partial_t B_r}$	$N_{\partial_t^2 B_r}$	$N_{\partial_t^3 B_r}$	VECT		SCAL		Global
					OBSY	CHAMP	Ørs.	CHAMP	SAC-C	
	(per 10^{12} nT^{-2})	(per 10^8 (nT yr^{-1})^2)	(per 10^5 (nT yr^{-2})^2)	(per 10^4 (nT yr^{-3})^2)	(nT yr^{-1})	(nT)	(nT)	(nT)	nT	(normalized)
gufm-sat-Q2	1.22	3.69	2.60	6.04	3.51	3.73	5.66	10.64	5.20	5.71	0.958
gufm-sat-Q3	1.22	3.72	4.19	1.24	3.53	3.72	5.66	10.67	5.13	5.70	0.957
gufm-sat-E3	1.29	5.37	4.33	1.25	3.53	3.73	5.67	9.79	4.93	5.71	0.958

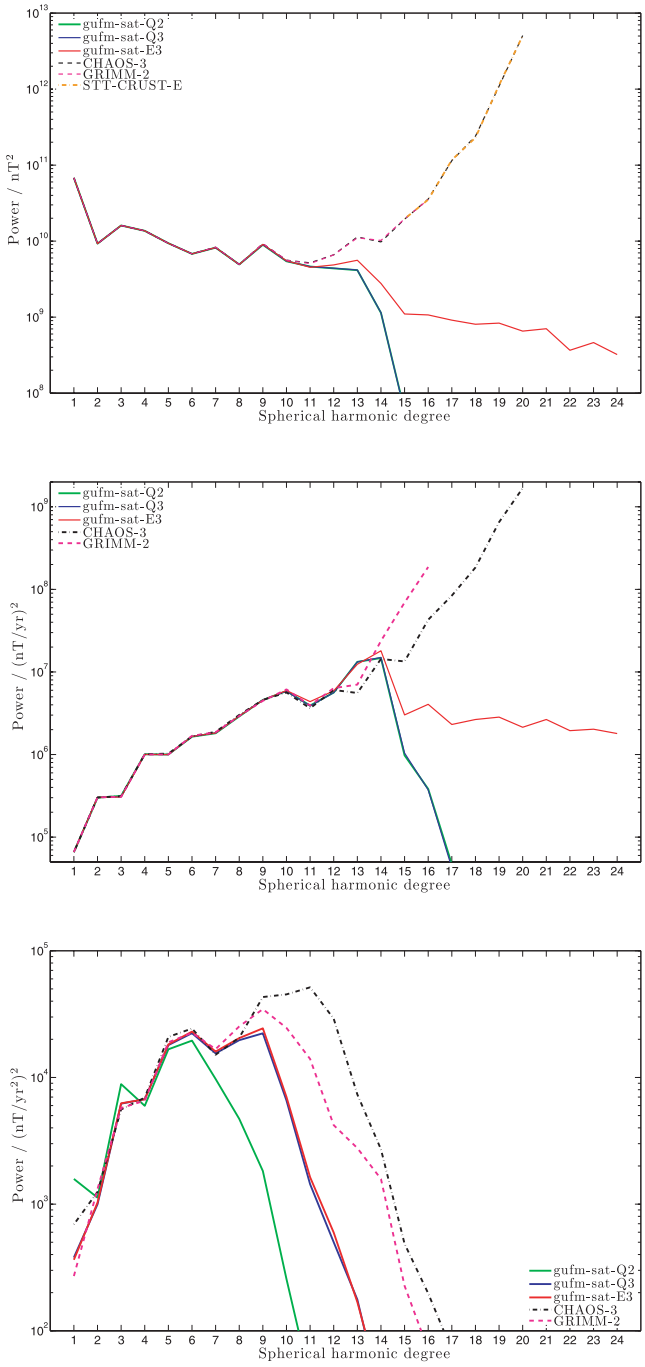

Figure 3. Spherical harmonic spectra in 2005.0 at the CMB for the MF (top plot), the SV (middle plot) and the SA (bottom plot). Models *gufm-sat-Q2* (green line), *gufm-sat-Q3* (blue line), *gufm-sat-E3* (red line) are shown along with *CHAOS-3* (black dot-dash line) and *GRIMM-2* (pink dashed line). The spectra of the *STT-CRUST-E* crustal field model is also plotted for degrees 15–24 as the orange line in the top plot.

for *gufm-sat-Q2*, after degree 9 for the *gufm-sat-Q3*, *gufm-sat-E3* and *GRIMM-2* models and after degree 11 for the *CHAOS-3* model. On the other hand *gufm-sat-Q2* has considerably more acceleration power in degree 1 than the other models. At observatories on Earth's surface this extra power is manifest as annual to interannual oscillations (Figs 6 and 7) that do not greatly improve the fit to the observatory data, leading to the suspicion that they may be spurious. It seems that the second time derivative

norm penalizes accelerations in degrees 6–10 of the field rather too strongly and that models constructed using it only manage to fit the satellite data adequately by allowing rapid oscillations of the degree 1 and 3 field. For this reason, in what follows, we choose to focus our interpretations on the *gufm-sat-Q3* and *gufm-sat-E3* models that possess fewer temporal oscillations at Earth's surface.

4.2 Evolution of model norms

We present the time evolution of four norms measuring field model complexity in Fig. 4. The norms investigated are the square of the radial field, the square of the first time derivative of the radial field, the square of the second derivative of the radial field and the square of the third time derivative of the radial field, respectively, in each case integrated over the CMB. Each plot compares the evolution of the norms for our three models *gufm-sat-Q2*, *gufm-sat-Q3* and *gufm-sat-E3*. All the models show a small increase (of ∼4 per cent) in the norm of B_r^2 between 2000.0 and 2010.0. Reasons for this minor systematic increase in complexity may include the decrease of CHAMP altitude over the decade, and also perhaps some incompatibility between the Ørsted and CHAMP data early in the decade. It seems unlikely that the core field itself has significantly increased in complexity over the short time interval studied. The entropy regularized model *gufm-sat-E3* has a higher value of this norm compared to *gufm-sat-Q2* and *gufm-sat-Q3* because in the latter models this norm is directly minimized. Considering the first time derivative norm, we again find that the entropy regularized model has a higher value than the quadratically regularized models. This is to be expected because it involves changes of a higher amplitude main field. Throughout the model span this norm displays only very minor changes in all the models; again this is as expected due to the imposed regularization and endpoint conditions. Turning to the second time derivative norm, we find this has smaller amplitude in *gufm-sat-Q2* where it is directly penalized, although rapid fluctuations are present in this case. All models show an increase from small values of SA at the endpoints to a maximum value around 2006. The increase and decrease in the norm is very smooth for *gufms-sat-Q3* and *gufm-sat-E3*, as is required by their third derivative regularization. Finally, considering the third time derivative norm we observe rapid, high amplitude, fluctuations for *gufm-sat-Q2* and a much lower value (with weak maxima in 2005 and 2007) for models *gufm-sat-Q3* and *gufm-sat-E3*. From these considerations, it seems that models *gufm-sat-Q3* and *gufm-sat-E3* possess more desirable properties and avoid the rapidly fluctuations in SA that are required by *gufm-sat-Q2*. Despite its drawbacks, we feel it is still of interest to discuss the latter model because its radial SA at the core surface is the minimum required to fit the data to the chosen level.

4.3 Maps and animations of the core surface field

Having considered global diagnostics of the field models, we next present maps of B_r and its first and second time derivatives at the core surface in 2005.0 in Fig. 5. Animations of the evolution of the radial MF, SV and SA of all the models are also available online at http://www.epm.geophys.ethz.ch/~cfinlay/gufm-sat/movies/. Such maps and movies provide direct insight into the geomagnetic field at the outer boundary of its source region, showing how it is organized and how it is evolving. The differences between the maps from the three models give an idea of the flexibility in producing models that satisfactorily fit the data. In Fig. 5 model *gufm-sat-E3* is always shown in the right column. In the top row maps of B_r in 2005 are presented, with model *gufm-sat-Q2* shown in the left

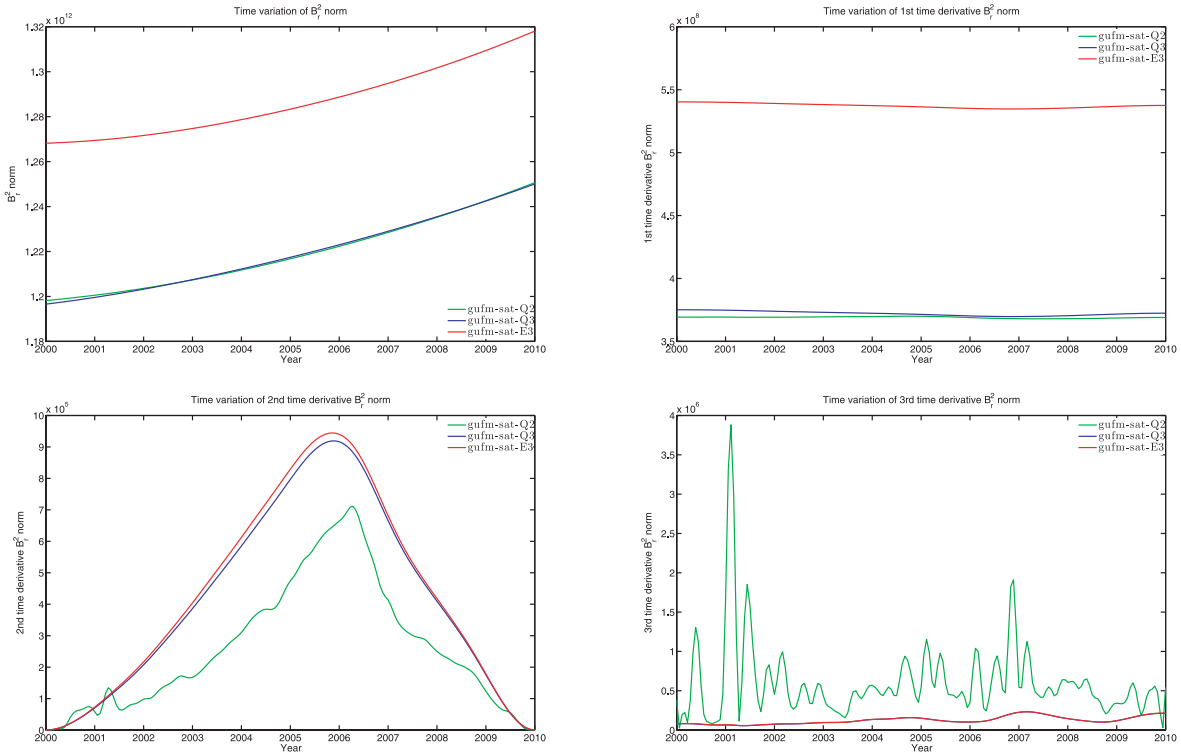

Figure 4. Comparison of time variation of model norms at the core surface. The green line shows *gufm-sat-Q2*, the blue line *gufm-sat-Q3* and the red line *gufm-sat-E3*. The top left plot shows the evolution of $\int_{\mathrm{CMB}} B_r^2 \, d\Omega$, the top right $\int_{\mathrm{CMB}} (\partial B_r/\partial t)^2 \, d\Omega$, the bottom left plot that of $\int_{\mathrm{CMB}} (\partial^2 B_r/\partial t^2)^2 \, d\Omega$ and the bottom right $\int_{\mathrm{CMB}} (\partial^3 B_r/\partial t^3)^2 \, d\Omega$.

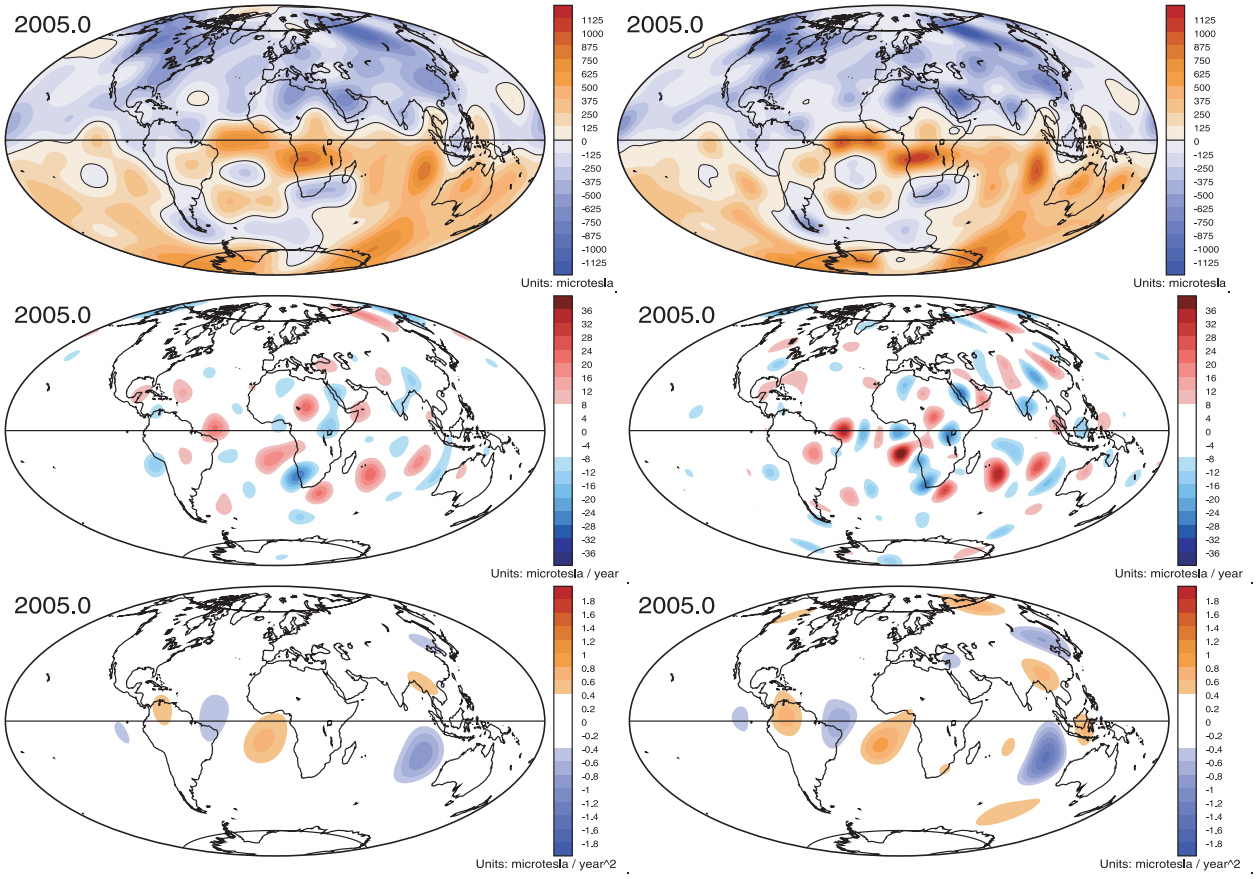

Figure 5. Contour plots of the radial MF (top panel), radial SV (middle panel) and radial SA (bottom panel) at the core surface in epoch 2005.0. The right column always shows *gufm-sat-E3*. In the left column, the top is the radial MF from *gufm-sat-Q2*, the middle is the radial SV from *gufm-sat-Q3* and the bottom is the SA from *gufm-sat-Q2*. Hammer-Aitoff projection is used; the tangent cylinder and the geographic equator are marked by solid black lines.

column. The map of B_r for *gufm-sat-Q3* is essential identical to that of *gufm-sat-Q2*. The maps obtained with respectively quadratic and entropy regularization show qualitatively similar structures. Both display the well known high latitude flux lobes and the large reversed flux patch in the Southern hemisphere stretching from below Africa over to below South America (Bloxham & Gubbins 1985; Gubbins & Bloxham 1987) as well as the low latitude wavetrain features north and south of the geomagnetic equator (Bloxham *et al.* 1989; Jackson 2003) under the Atlantic hemisphere. The amplitude of the flux concentrations is higher in the entropy regularized models as was found in previous studies (Jackson 2003; Gillet *et al.* 2007; Jackson *et al.* 2007). Low flux regions are found above the north geographic pole. There are generally fewer intense MF features under the Pacific hemisphere. Large amplitude undulations of the magnetic equator in the region under Indonesia are present in all the models. Comparing the *gufm-sat-Q2* and *gufm-sat-Q3* models (top left hand side) to the *gufm-sat-E3* model (top right hand side) we observe that some of the weaker reversed flux patches seen in the 'gufm-sat-Q' models disappear in the *gufm-sat-E3* model, despite the latter fitting the data equally well. This illustrates that the exact morphology of weak reversed flux patches is not precisely known and depends on the *a priori* choice of regularization norm (or truncation level); such weak flux features should therefore be interpreted with caution (see also Wardinski & Lesur 2012).

The middle row of Fig. 5 presents the radial component of SV at the core surface. Its right column shows *gufm-sat-E3* while the left column shows *gufm-sat-Q3*. The SV map for *gufm-sat-Q2* is essentially identical to that shown for *gufm-sat-Q3*. The most striking aspect of the SV maps is that the most intense sites of field change are located almost exclusively under the Atlantic hemisphere. Furthermore, field change is strongest at low to mid latitudes, as also observed during the past 400 yr (Jackson *et al.* 2000; Finlay & Jackson 2003). Much of this SV is today associated with the development of the low latitude wavetrain features. Here, using high quality satellite data with good spatial and temporal coverage, we provide strong support for the hypothesis that SV is weaker under the Pacific region. Further discussion of this point is postponed until Section 5.3. Strong SV is also seen clearly near the tangent cylinder around the inner core, especially in the northern hemisphere under Siberia and Alaska; equivalent features are not found in our models under the southern hemisphere. As previously noted by Holme *et al.* (2011) it is also remarkable that within the tangent cylinder, at very high latitudes in both the Arctic and Antarctic, the SV is of lower amplitude than outside the tangent cylinder. This is particularly striking in model *gufm-sat-Q3* but is also evident in *gufm-sat-E3*. The primary difference between the SV maps in the entropy and quadratic regularized models is that the former possesses features with higher amplitude and sharper edges.

The bottom row of Fig. 5 presents the radial component of SA at the core surface. The right column again shows *gufm-sat-E3* while the left column shows *gufm-sat-Q2*. The SA map for *gufm-sat-Q3* is very similar to that shown for *gufm-sat-E3*. Note that for the MF and SV, models with the same spatial regularization were essentially identical; but here it is the form of temporal regularization

that determines whether or not similar SA maps are obtained. Large scale, high amplitude, structures are evident for models with both second and third time derivative regularization; this encourages us to argue they are robust and can be interpreted. Most of the dominant features are found at mid to low latitudes under the Atlantic hemisphere, and they are again apparently related to the evolution of the wavetrain flux features. In 2005.0 the most prominent structure is a large patch of negative acceleration under the eastern Indian Ocean which is present in all the *gufm-sat* models. Another strong SA feature is seen under Siberia in *gufm-sat-E3* in 2005 but is less prominent in *gufm-sat-Q2*. What is not evident from considering such a snapshots is the difference in the temporal evolution of the SA between the models with second and third derivative damping. To obtain the same level of misfit, model *gufm-sat-Q2* has much greater fluctuations in the amplitude of its SA features; in contrast, the models with third time derivative regularization show a gradual evolution in the SA amplitude from values close to zero at the endpoints up to a maximum value in 2006. The artificial forcing of SA to zero at the endpoints is unfortunate, and certainly unphysical. It is the cause of undesirable end effects in our models and those of other workers. However, we have carried out extensive tests showing without this constraint too much power enters into the small scale SA which is possibly an even worse problem. Further work is needed on new approaches to resolve this shortcoming.

4.4 Fit to annual differences of observatory monthly means

A crucial test of the quality of any geomagnetic field model is how well it fits ground observatory data. In Figs 6 and 7 we present examples of the fit of the *gufm-sat-Q2*, *gufm-sat-Q3* and *gufm-sat-E3* models as well as *CHAOS-3* (which spans 1997.0–2010.0) and *GRIMM-2* (which spans 2001.0–2009.5) to annual differences of the processed monthly means data described in Section 2.2. The X, Y and Z components are shown at two observatories located in continental interiors [Tamanrasset, (TAM) in Algeria and Novosibirsk/Klyuchi (NVS) in Russia] in Fig. 6, and at two observatories located on islands [Martin de Vivies/Amsterdam Island (AMS) in the southern Indian ocean and Honolulu (HON) Island in the Pacific Ocean] in Fig. 7. The five models plotted largely agree in their trends and their changes in slope. Differences between the *gufm-sat* models and *CHAOS-3* and *GRIMM-2* are partly due to the different start and end points of the models, and also because *GRIMM-2* uses observatory hourly means rather than monthly means as input data. Due to the large number of hourly data, this effectively gives more weight to the observatory data. Summary statistics for the fit of the models to the observatory data are presented in Table 1.

Model *gufm-sat-Q2* displays notable short-period oscillations with amplitude a few nT yr^{-1}. These ascillations are especially visible, for example, in the Z components at NVS and AMS, and in the X and Z components at HON. They are not present in the other models which are regularized by penalizing the third time derivative. Furthermore, these oscillations do not greatly improve the fit to observatory data. They are also generally weaker in the Y component indicating their origin in oscillations of the zonal ($m = 0$) components of *gufm-sat-Q2*. This, together with the comparatively large power in degrees 1 and 3 in *gufm-sat-Q2*, suggests that in this model either that external field variations are being incorrectly mapped into the core field or else that the polar data gap in winter is causing spurious temporal oscillations that are not adequately controlled.

Histograms of the residuals between *gufm-sat-E3* and annual differences of the processed observatory monthly means are presented in Fig. 8. Combining the residuals from all observatories, dX/dt, dY/dt and dZ/dt all possess very small mean residual values, and

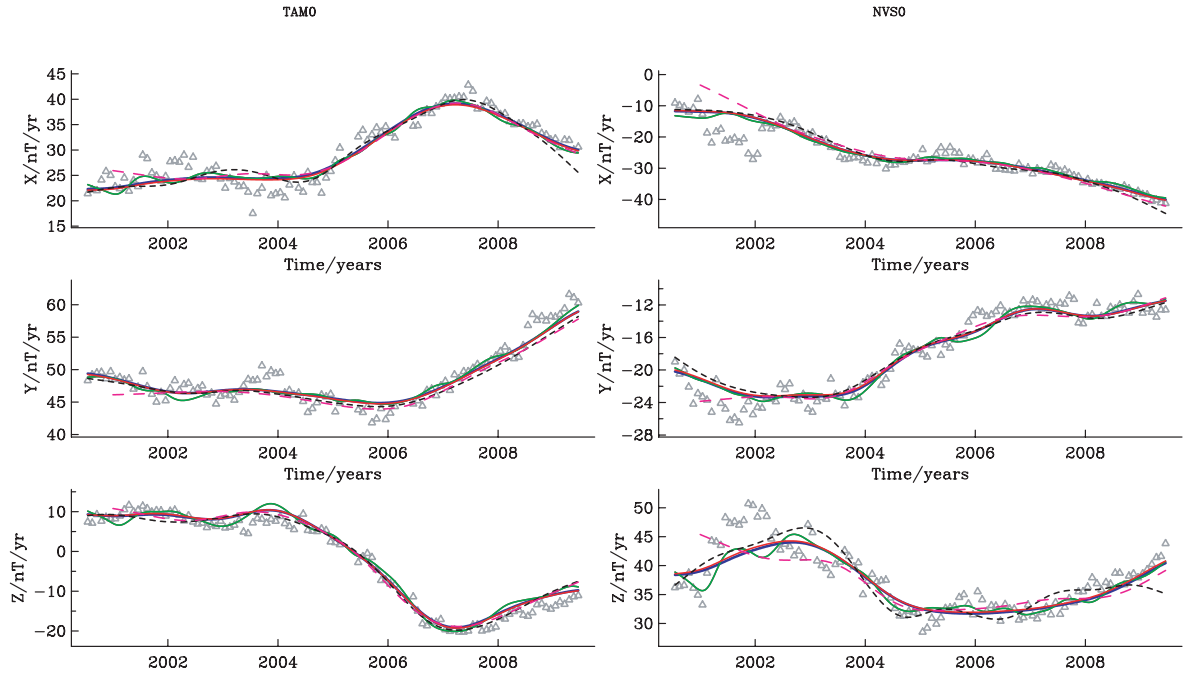

Figure 6. Comparison of model predictions at Earth's surface with annual differences of month means (grey triangles) at Tamanrasset, Algeria (left hand side) and Novosibirsk/Klyuchi, Russia (right hand side) magnetic observatories. First time derivatives of X, Y and Z are shown in the top middle and bottom rows, respectively. The green solid line is *gufm-sat-Q2*, blue solid line is *gufm-sat-Q3*, red solid line is *gufm-sat-E3*, black dashed line is *CHAOS-3* and pink dashed line is *GRIMM-2*. Note that lines may overlap.

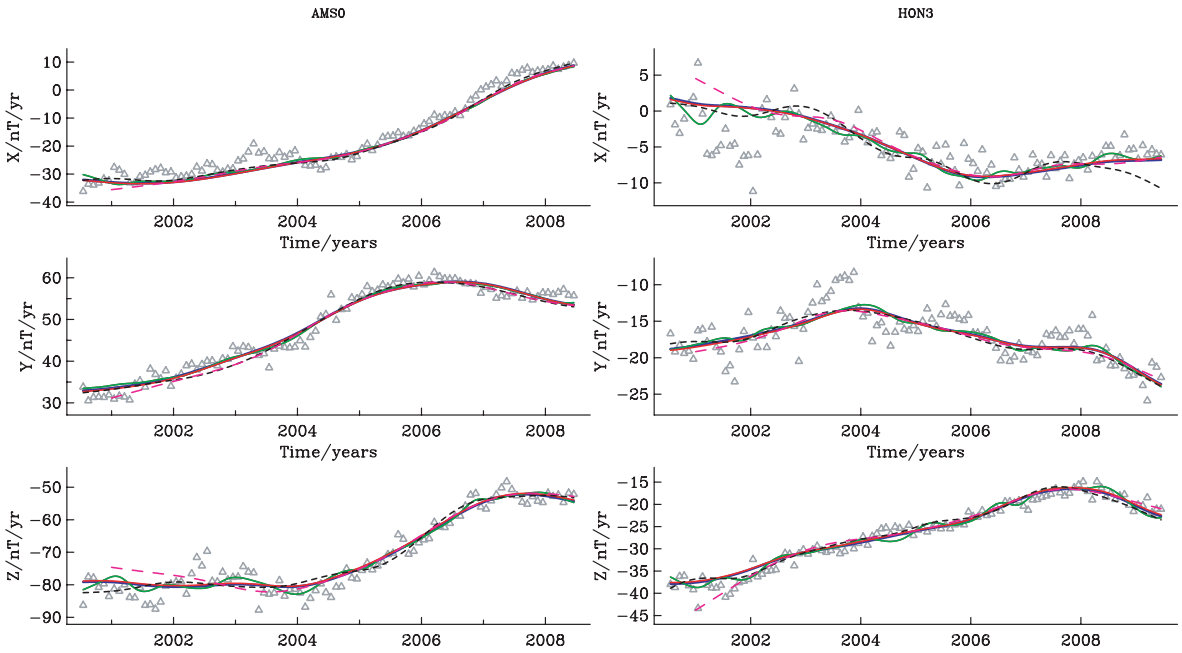

Figure 7. Comparison of model predictions at Earth's surface with annual differences of month means (grey triangles) at Martin de Vivies/Amsterdam Island, French Australian and Antarctic Territories (left hand side) and Honolulu, U.S.A (right hand side) magnetic observatories. The green solid line is *gufm-sat-Q2*, blue solid line is *gufm-sat-Q3*, red solid line is *gufm-sat-E3*, black dashed line is *CHAOS-3* and pink dashed line is *GRIMM-2*. Note that lines may overlap.

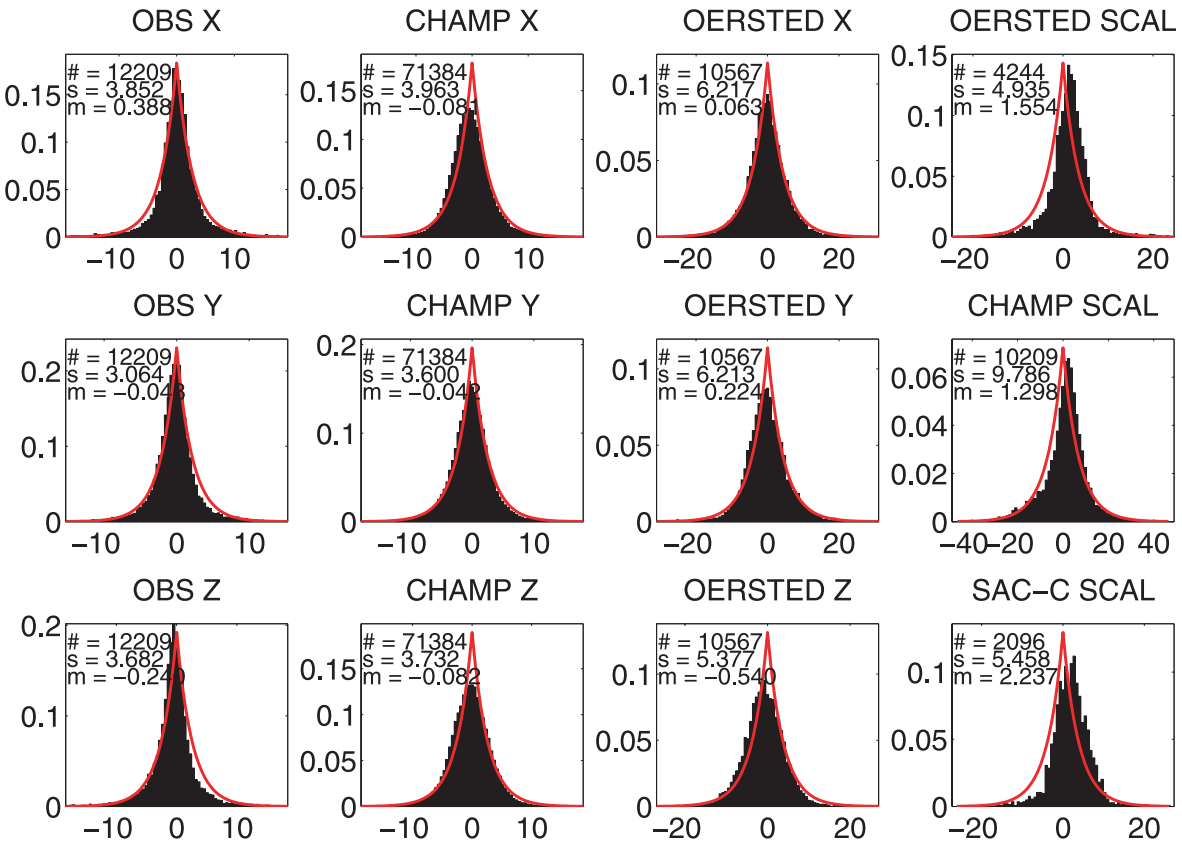

Figure 8. Histograms of residuals between the *gufm-sat-E3* model and the satellite and observatory data sets used for the model construction. Units are in nT except for the observatory data where units are nT yr^{-1}. m denotes mean residual value, s denotes an L_1 measure of spread in each case. The red lines show Laplacian distributions with this spread but zero mean. Also noted on each plot is the number of contributing data.

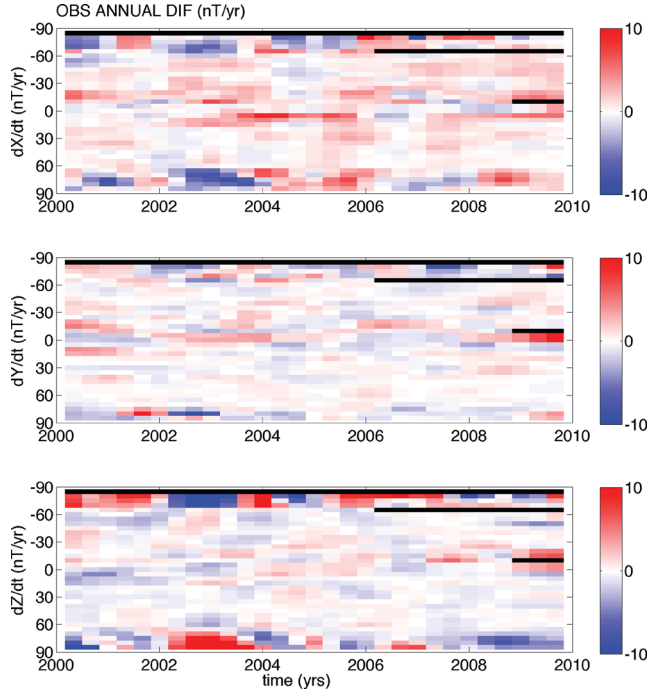

Figure 9. Time–geomagnetic latitude plot of the mean residual between the *gufm-sat-E3* model and the annual differences of observatory monthly means used for the field modelling. Bin widths are 3 months in time and 5° in geomagnetic latitude. Black indicates no data is available for this time and location. Units are nT yr^{-1}.

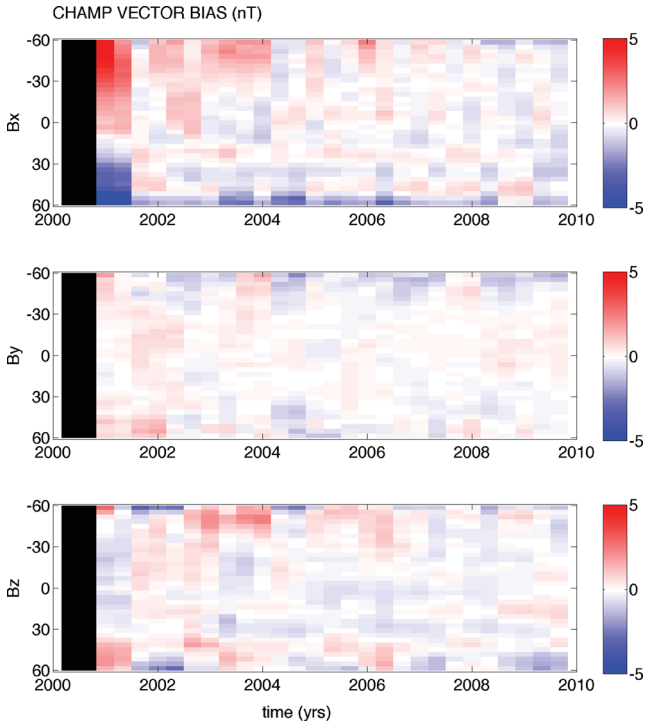

Figure 10. Time–geomagnetic latitude plot of the mean residual between model *gufm-sat-E3* and the CHAMP vector data used for model construction. Bin widths are 3 months in time and 5° in geomagnetic latitude. Black indicates no data exist for this time and location. Units are nT.

their distributions are approximately Laplacian. The width of the residual distribution is smallest for the Y component and largest for the X component. In Fig. 9, residuals between the predictions of *gufm-sat-E3* and the observatory data are plotted as a function of time and geomagnetic latitude to study their space-time characteristics. All residuals falling within a specified time-geomagnetic latitude window (3 months by 5°) are averaged and the result determines one pixel in the plot. We find mean residuals in dY/dt are mostly small, except occasionally at low geomagnetic latitudes (e.g. in 2009) or at high geomagnetic latitudes (e.g. in 2002). Because this component is expected to be least influenced by ring current fluctuations, it is encouraging that it is well fit by *gufm-sat-E3*. Considering dX/dt and dZ/dt, large amplitude residuals are consistently observed at high geomagnetic latitudes. It is noteworthy that residuals in dX/dt show a pattern that is mostly symmetric about the geomagnetic equator while those in dZ/dt are approximately antisymmetric about the geomagnetic equator, that is, the residuals are of opposite signs in the north and south hemisphere at any given time. This type of symmetry would be produced by unmodelled fluctuations of an external dipole magnetic field, that have not been completely removed from our processed observatory data set. It is also noteworthy that the residual variations have a time scale of approximately 6 months to 1 yr, after which a change in sign is often observed.

4.5 Fit to satellite data

Histograms of the residuals between *gufm-sat-E3* and satellite data separated into vector and scalar components and by satellite are presented in Fig. 8. The residuals from the CHAMP vector satellite data (which constitutes the vast majority of the data used) have almost zero mean values. The Ørsted vector data have larger residuals than the CHAMP data, as expected because it had only one star camera head and because it was only used in this study when there were gaps in the coverage of CHAMP data. The Ørsted and SAC-C scalar data have mean values of order + 1.6 nT and 2.2 nT, respectively, which are larger than those for the CHAMP scalar data; but note that these scalar data are primarily from high latitudes where stronger unmodelled effects are expected. We have also examined similar histograms of residuals between the *gufm-sat-E3* model and the remaining part of the *CHAOS-3* data (with external and crustal field estimates removed as described in Section 2.1) that was not used for modelling in this study. This effectively constitutes a large independent data set that we are able to use for testing and evaluation purposes. We find very similar results for the vector data, with mean values close to zero and measures of spread less than 0.3 nT larger than those shown in Fig. 8 for the CHAMP vector data. We also found mean values of less than 0.5 nT, and spreads less than 0.4 nT larger than those shown in Fig 8 for the Ørsted vector data. Comparison with unused scalar data is more difficult because much of it comes from high latitudes. We find that the residuals from the unused CHAMP scalar data show a negative mean value and a skewed distribution, while the unused Ørsted and SAC-C scalar data have a positive mean value of around 2.5 nT. This unused data suggests that model *gufm-sat-E3* generally does a good job of fitting satellite vector data at mid and low latitudes but that there are unresolved difficulties in fitting the more disturbed high latitude scalar data.

In Fig. 10 we present a time-geomagnetic latitude plot of the mean residuals between CHAMP vector data used in the inversion and *gufm-sat-E3* in 3 month by 5° bins. The residuals are observed to become systematically larger as auroral latitudes are approached (as we had anticipated in our choice of error estimates) with the X and

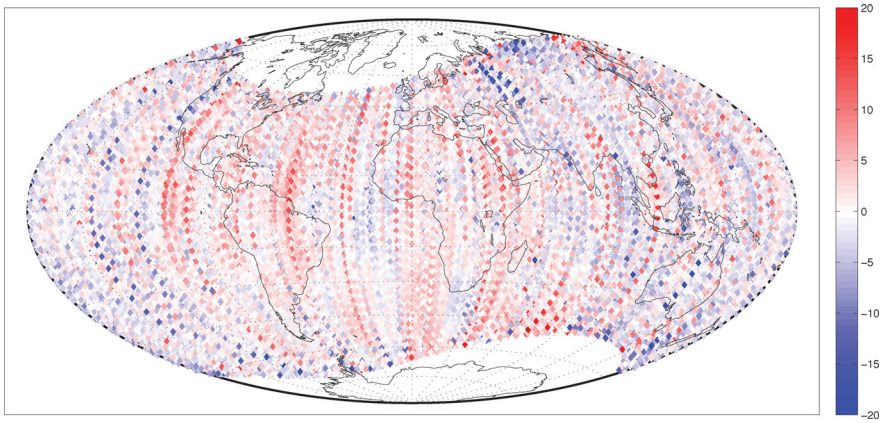

Figure 11. Geographical plot of residuals between the *gufm-sat-E3* model and CHAMP vector *Y* component data in 2008 from the *CHAOS-3* data set (with estimates of the magnetospheric field and the accessible part of the crustal field removed) that were not used for model construction. Units are nT.

Z components being more notably noisy than the *Y* component. The residuals are generally smaller in amplitude after 2006, as the quiet conditions of solar minimum are reached. A strong enhancement in the residuals for the CHAMP vector data is clearly evident in the first half of 2001. This could be because the CHAMP vector data are less accurate during this initial interval (prior to mid 2001, approximately Julien day 500, the CHAMP vector data were in an engineering stage so are not expected to have as high accuracy as later data), but may also partly be due to incompatibilities between the CHAMP vector data and the other data sources which dominated before CHAMP vector data were available. Very similar patterns are found when data not used for the model construction is examined in the same way.

In Fig. 11 we present an example of the geographical distribution of residuals between the *gufm-sat-E3* model and CHAMP *Y* component data from the year 2008, that were not used for the model construction. It is evident that there is an excellent coverage of vector data at low and mid-latitudes in 2008. The majority of the residuals have values less than $\pm$ 5 nT. The remaining residuals with higher amplitudes are, however, not completely random. It is clear that certain tracks are more disturbed; this hints that a track-by-track data selection criteria could be useful in the future. In addition, there appear to be regions close to the auroral zone (especially over Siberia, over North America, over the Southern Atlantic, and over a region south of Australia) where higher amplitude residuals are systematically more likely. It is remarkable that these are also regions where the main field is strongest in the ionosphere, perhaps contributing to larger induced ionospheric currents in these locations.

4.6 Comparison of model global norms and misfits

In Table 1 statistics of the global properties of the *gufm-sat* models including model norms, misfits to different data set and global misfits, are collected for reference and comparison. In terms of global misfit, there is very little to choose between the three models. In terms of model norms, *gufm-sat-E3* has a larger B_r^2 norm, because use of an entropy norm does not directly suppress high amplitude radial field. Nonetheless, *gufm-sat-E3* is very well suited for interpretation of B_r maps at the core surface, because it is well converged at this radius but not drastically smoothed by spectral truncation or quadratic regularization. If one on the other hand prefers a more cautious model with lower field amplitudes that gives the same fit to the data, then *gufm-sat-Q2* or *gufm-sat-Q3* may be favoured. If a user wishes to interpret the SA at the core surface then model *gufm-sat-Q2* may be worth considering, because it has the minimum amplitude of SA needed to fit the observations. On the other hand, in order to fit the data to the same level as *gufm-sat-Q3* and *gufm-sat-E3*, *gufm-sat-Q2* requires significant temporal oscillations of its low degree harmonics that we believe may be spurious. By presenting three models we wish to provide readers with a feeling for the flexibility modellers have in producing solutions that are compatible with observations. The model finally preferred depends on *a priori* opinions concerning what is physically reasonable at the core surface, and also the intended use for the model. Henceforth we shall use *gufm-sat-E3* for our discussions and interpretations.

5 DISCUSSION AND IMPLICATIONS FOR CORE PROCESSES

5.1 Low latitude wavetrains and rapid field change under the eastern Indian ocean

A series of intense flux patches at low latitudes north and south of the geomagnetic equator (Jackson 2003) has been observed to drift westwards over the past 400 yr (Bloxham *et al.* 1989; Jackson *et al.* 2000; Finlay & Jackson 2003). This wavetrain feature underlies much of the westward drift observed at Earth's surface (Bullard *et al.* 1950) and is thus one of the most important aspects of today's geomagnetic field evolution. In this study, we have extended the high resolution snapshot obtained by Jackson (2003) to investigate how this feature has developed between 2000 and 2010. Even over this short 10 yr interval, its components are clearly observed to move westwards. Westward motion is especially evident (e.g. in *gufm-sat-E3*) for the flux patches located under northern Australia, the eastern Indian Ocean, Arabia, central Africa, the mid-Atlantic and central South America. The strong oscillatory features under Indonesia on the other hand do not drift during this time, as was previously noted in earlier historical studies (Bloxham & Gubbins 1985). We further find that locations of the most intense SV and SA often occur near the edges of the highest amplitude, fastest westward moving, patches in the wavetrain.

Rapid field evolution has recently been reported at Earth's surface in the eastern Indian Ocean (Olsen & Mandea 2008; Lesur *et al.* 2008). Because the *gufm-sat* models are regularized in both space and time at the core surface, it is possible to use them to examine the (large scale) origin of this phenomenon at the core surface. We find that between 2000 and 2010 a flux concentration located

under the Cocos Islands has intensified, grown in size and started to move westwards. It seems that we may be witnessing the birth of the latest member of the low latitude wavetrain south of the geomagnetic equator, and the early stages of its westward drift. Its rapid evolution is also evident in the radial SV and SA at the core surface. Our models show a positive patch of radial SV west of the MF patch under the Cocos Island, indicating where flux is being moved towards, and a negative radial SV patch to the south east, where the amount of radial flux has decreased. Because the amplitudes of the SV patches in this region have themselves changed (the negative SV patch has strengthened while the positive patch has weakened in the past 10 yr), a strong pulse of negative radial SA is present in this region between 2002 and 2008.

Examination of core surface field evolution over the past 400 yr using the *gufm1* model (Jackson *et al.* 2000) indicates that the activity under the Cocos Islands in the past 10 yr is not the first episode when normal flux has been concentrated at low latitudes in this region before moving westwards. In 1590, *gufm1* shows a strong normal flux patch at low latitudes south of India which subsequently moves westwards and eventually becomes the strong normal flux patch presently under central Africa. Furthermore, between 1830 and 1930, normal flux appears to have been transported northwards from the flux lobe to the east of Antarctica to form a normal flux patch at low latitudes under the eastern Indian Ocean. This patch subsequently split, with some flux remaining close to the region under the Cocos Islands, and the remainder moved rapidly westwards to form the strong patch today located beneath the Maldives and the Seychelles. Intriguingly, there is also tentative evidence from time-averaged palaeomagnetic field models (e.g. Gubbins & Kelly 1993) that non-axisymmetric normal flux has often been concentrated in this region of the eastern Indian Ocean. It seems that the high quality global data available in the past 10 yr has enabled us to image in unprecedented detail the latest episode in this process.

These observations motivate us to conjecture the following mechanism for the operation of the low latitude wavetrains. We propose that flux patches making up the wavetrain features north and south of the geomagnetic equator are created around 100° east where episodic bursts of meridional flow transports flux from the high latitude lobes towards lower latitudes. Close to the equator this strong flow turns westwards and carries flux beneath Africa and Europe until, under the Americas, it diverges back towards the poles. Thus we envisage a planetary scale gyre acting as conveyor belt transporting flux from high latitudes (where it is created by the geodynamo process), concentrating it at low latitudes, and then carrying it westward under the Atlantic hemisphere. This process is currently most obviously operating south of the geomagnetic equator, where flux of the same polarity as the nearby high latitude lobe is rapidly being concentrated under the eastern Indian Ocean. It may however also be operating in the northern hemisphere in the formation of flux concentrations under eastern Asia. Such a planetary scale gyre, symmetric about the equator, with strong equatorward flow at 100° east, and westward flow under the Atlantic hemsphere, is precisely what is indicated in recent quasi-geostrophic core flow inversions (Pais & Jault 2008; Gillet *et al.* 2009, 2011). A plot showing the gyre structure obtained in these studies, with geographical features marked allowing easy comparison to our maps of B_r, may be found in fig. 8 of Finlay *et al.* (2010). Further evidence in support of such a gyre (at least south of the equator) can also be found in many other core flow models, for example, the tangentially geostrophic flows of Jackson (1997), the tangentially geostrophic and toroidal flows of Holme & Olsen (2006), and the helical flows of Amit & Olson (2006). This feature also appears to have existed at least for the past few centuries (e.g. Bloxham 1992). Within this scenario, rapid field accelerations in the vicinity of the eastern Indian Ocean [see Fig. 5 and also Olsen & Mandea (2007) and Chulliat *et al.* (2010)] can be attributed to episodes of enhanced equatorward flow; the gyre is evidently not completely steady, but rather punctuated by bursts of activity. This provides a simple explanation for the meridional flow accelerations inferred from satellite data in this region by Olsen & Mandea (2008).

The ultimate dynamical origin of this flux conveyor belt, and the reason for its current position is uncertain. It may be an outcome of thermal core–mantle coupling and related to the present configuration of heat transport in the deep mantle (Christensen & Olson 2003), or it may simply be a consequence of magnetostrophic balance (Gillet *et al.* 2009), due to thermal or magnetic winds associated with the configuration of buoyancy and magnetic fields in today's geodynamo (Dumberry & Bloxham 2006). The low latitude wavetrain observed in our field models has intriguing similarities to some aspects of the field evolution patterns seen at low latitudes in the UHFM geodynamo simulation of Sakuraba & Roberts (2009). In this high resolution simulation, movies show that flux is episodically stripped from the high latitude lobes by meridional flows, and deposited at lower latitudes before being transported westwards by strong thermal winds. Although very impressive, the simulation of Sakuraba & Roberts (2009) possesses stronger equatorial antisymmetry than today's geodynamo (see later) and does not involve any longitudinal hemispheric asymmetry. Further study of simulations in a similar regime, but with higher Rayleigh number and with inhomogeneous heat flux boundary conditions are needed to shed more light on the mechanics of the low latitude wavetrains.

Although we favour a gyre based mechanism for the formation and evolution of the low latitude wavetrains, on the grounds that it is a parsimonious explanation consistent both with results from frozen-flux flow inversions and with the thermal winds driven by inhomogeneous heat flux boundary conditions (Olson & Christensen 2002; Christensen & Olson 2003; Aubert *et al.* 2007), other explanations cannot be ruled out. For example, one could imagine strong shear producing toroidal field at depth in the core, and it then being transported to the core surface by a buoyant upwelling, before diffusing across the CMB as an intense patch of radial field (e.g. Gubbins 1996; Amit & Christensen 2008; Sreenivasan & Gubbins 2008). This process may conceivably excite slow magnetohydrodynamic waves that could propagate westward before dissipating. Such production of radial flux was found to occur preferentially at low latitudes near Indonesia in the numerical dynamo simulations studied by Sreenivasan & Gubbins (2008). But to the best of our knowledge, the wave propagation part of this scenario has not yet been documented in self-consistent dynamo simulations.

5.2 Origin of the decaying axial dipole

The aspect of present field evolution of greatest public interest is undoubtedly the ongoing decay of the intensity, as diagnosed by the amplitude of the axial dipole moment. This phenomenon has been linked to the growth and migration of reversed flux features in the Southern hemisphere (Bloxham & Gubbins 1985; Gubbins 1987; Gubbins *et al.* 2006) and also to the equatorward motion of normal flux concentrations (Olson & Amit 2006). Do our models provide any additional insight into how this process has occurred during the past 10 yr? Fig. 12 presents the rate of change of the axial dipole in the *gufm-sat* models between 2000 and 2010 with the *CHAOS-3* and *GRIMM-2* models also shown for reference. All models agree

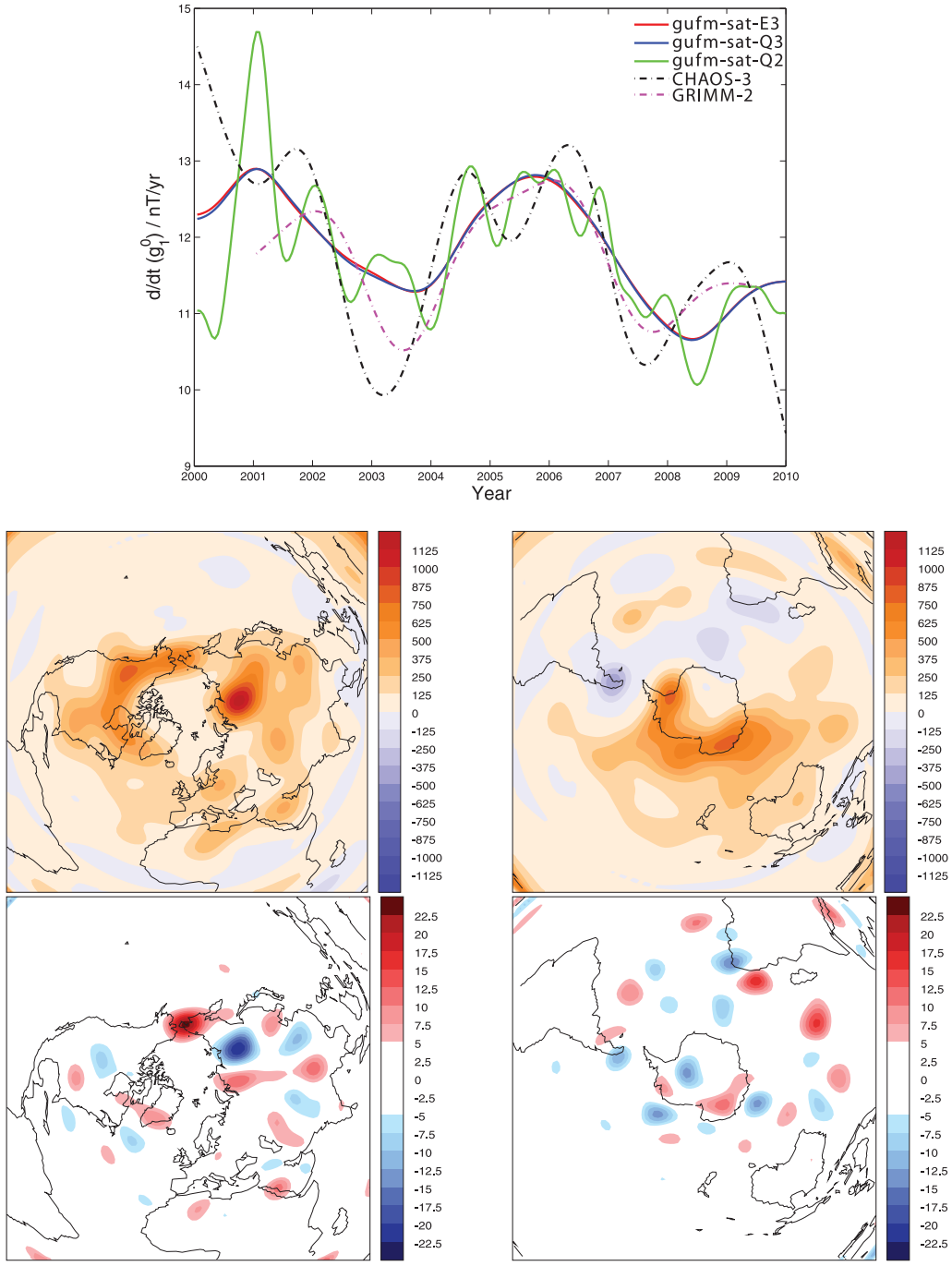

Figure 12. Top panel shows the rate of change of axial dipole between 2000.0 and 2010.0 in the *gufm-sat* models, with *CHAOS-3* and *GRIMM-2* also shown for reference. The middle row shows $Z\cos\theta$, which gives rise to the axial dipole when integrated over the core–mantle boundary, from *gufm-sat-E3* in 2005.0, (orange-blue scale indicating positive and negative contributions to the amplitude of the axial dipole). The bottom row shows the instantaneous time derivative of $Z\cos\theta$ documenting the contributions to the rate of change of the axial dipole (red–blue scale indicating contributions to growth and decay of the axial dipole). Left column shows the north polar region, right column shows the south polar region both in Lambert equal area projection.

in an average rate of axial dipole decay of $\sim$12 nT yr^{-1} or 4 per cent per century. Our preferred models *gufm-sat-Q3* and *gufm-sat-E3* suggest that the rate of axial dipole decay has actually slightly slowed from $\sim$13 to $\sim$11 nT yr^{-1} in the past 10 yr, although there are significant oscillations about that trend. *gufm-sat-Q2* displays much larger oscillations in its axial dipole than the other models, especially around 2001, but as discussed earlier we suspect these oscillations may be spurious.

In Fig. 12 contributions to the axial dipole, and its rate of change in 2005.0, are presented by plotting $Z\cos\theta$ and its time derivative. These plots are equal area projections centred on the poles in the northern and southern hemispheres, respectively. Comparison with similar maps for epoch 1945.0 presented by Gubbins (1987) dramatically illustrates the increase in knowledge of core surface field that has taken place with the advent of satellite observations. In 1945 the major contribution to the decay of the axial dipole

were large scale negative features seen in the time derivative of $Z\cos\theta$ under southernmost South Africa and southernmost South America. These were interpreted as a consequence of the growth and southward motion of the reversed flux patches under South Africa and South America (Gubbins 1987). In 2005, although the axial dipole decay was still clearly continuing, the situation is apparently more complex, perhaps because smaller scales of the SV can now be resolved. In the northern hemisphere the positive and negative contributions (though they are individually large) approximately cancel out contributing only 1.2 nT yr^{-1} to the decay rate of 12.5 nT yr^{-1}. As in 1945, it is primarily in the southern hemisphere (contributing the other 11.3 nT yr^{-1} in 2005.0) where the dipole decay originates. We find that the reversed flux features under southernmost South America and South Africa do indeed make a negative contribution to the change in the axial dipole, but a number of other features also play important roles. It should be emphasized that it is not just reversed flux features that are involved; weakening and equatorward flux transport from the high-latitude normal flux lobes (Olson & Amit 2006) also clearly plays a role, for example, west of Australia. Numerous subtle changes in the southern hemisphere field morphology combine to produce the current dipole decay. It should also be recognized that further changes may occur at even smaller length scales that cannot yet be resolved.

The observed dipole decay in 2005 seems to favour a mixed advection–diffusion mechanism as proposed by Olson & Amit (2006). Following Gubbins (1987, 1996), and using insight gained from numerical dynamo simulations, they argued that convective upwellings can transport reversed field from deep in the core, inducing large radial field gradients close to the CMB, and that radial diffusion can then result in rapid field changes at the core surface. However, they also emphasized that meridional flows can redistribute flux (e.g. normal flux from the high latitude lobes) by advection, also making significant contributions to changes in the axial dipole. Although our models of core surface field evolution are limited to the past decade, they are compatible with both of these mechanisms contributing to the present axial dipole decay. More detailed deterministic models of the such a scenario, including important predictions of its future behaviour, will thus unfortunately require knowledge of both the field and flow within the core. Although currently beyond reach, data assimilation methods (Fournier *et al.* 2010) may eventually allow progress in this direction.

5.3 Pacific–Atlantic hemispheric asymmetry

The excellent spatial and temporal coverage of observations in the past decade provides us with an ideal opportunity to re-examine some fundamental questions concerning the structure of the geomagnetic field and its evolution mechanisms. One long standing question has been whether the Pacific and Atlantic hemispheres possess a fundamentally different MF structure, and whether the fields in the two hemispheres evolve in a different manner (Fisk 1931; Doell & Cox 1971; Bloxham & Gubbins 1985; Walker & Backus 1996). In Fig. 13 the radial component of the MF, SV and SA in 2005.0 from model *gufm-sat-E3* are plotted at the core surface in a Hammer-Aitoff projection centred on longitude 180°. It is striking that both the radial SV and the SA are weak in the Pacific. This is the case for all the *gufm-sat* models and has also been observed in previous satellite field models (Hulot *et al.* 2002) and the latest CHAOS field models when these are truncated at degree 13 (Holme *et al.* 2011). In the MF, although there are some westward moving low latitude field concentrations in the central Pacific hemisphere, these features are of much smaller amplitude than those found in the Atlantic hemisphere, and hence their motions do not generate a large amount of SV or SA.

One primary distinction between the Pacific and Atlantic hemispheres is that the intense low latitude flux patches are less visible in the Pacific hemisphere. This may be a consequence of the mechanism by which these patches are formed in the eastern Indian Ocean (Section 5.1) before moving westward. Testing whether the combination of core flow configuration and main field morphology producing the present hemispheric asymmetry is merely a coincidence due to the current arrangement of convection cells in Earth's core (Kuang & Bloxham 1998; Hulot *et al.* 2002), or whether it is a consequence of inhomogeneous heat flux into the mantle or CMB topography modulating convection (Hide 1967; Christensen & Olson 2003; Gubbins & Gibbons 2004), requires accurate observations over a much longer time span than is available for this study.

5.4 Equatorial symmetry of the core surface field

In Fig. 14 we present a decomposition of the radial field at the core surface in 2005.0 from the *gufm-sat-E3* model into its equatorially symmetric (E^S) and equatorially antisymmetric (E^A) parts (e.g. Gubbins & Zhang 1993). Both maps have the same colour scale, so it is instantly apparent that the present field contains not only strong E^A components (sometimes referred to as the dipole family) but also strong E^S components (sometimes called the quadrapole family). The geographical distribution of energy in the E^S component is also very distinctive—it is maximum at low latitudes and under the Atlantic hemisphere.

Some prominent flux features are predominantly of one symmetry, for example, the high latitude flux lobes under North America, Siberia and east and west of Antarctica are predominant E^A. Other features, such as the low latitude wavetrains north and south of the geomagnetic equator, are composed of almost equal quantities of both symmetry classes. A consequence of this is that geodynamo models possessing primarily one symmetry (e.g. E^A) will be unable to correctly reproduce such phenomenon. The presence of both symmetries in geodynamo simulations requires sufficiently hard driving (i.e the Rayleigh number being sufficiently super-critcial) though this usually brings with it other undesirable features associated with inertia becoming important in the dynamics, for example, loss of the strong axial dipole and frequent reversals. The challenge of producing both an Earth-like field geometry and having core dynamics as close as possible to that expected for Earth (low Ekman number, low Rossby number, low magnetic Prandtl number) remains difficult.

6 CONCLUDING REMARKS

We have presented the *gufm-sat* field models that describe the evolution of the geomagnetic field at the core surface between 2000.0 and 2010.0. They are constrained by CHAMP, Ørsted and SAC-C satellite observations extracted from the *CHAOS-3* data set of Olsen *et al.* (2010), and by measurements from the global ground observatory network. The *gufm-sat* models minimize measures of both spatial and temporal field complexity at the core surface, and they contain less power in the MF beyond spherical harmonic degree 11 than other models which are not spatially regularized at

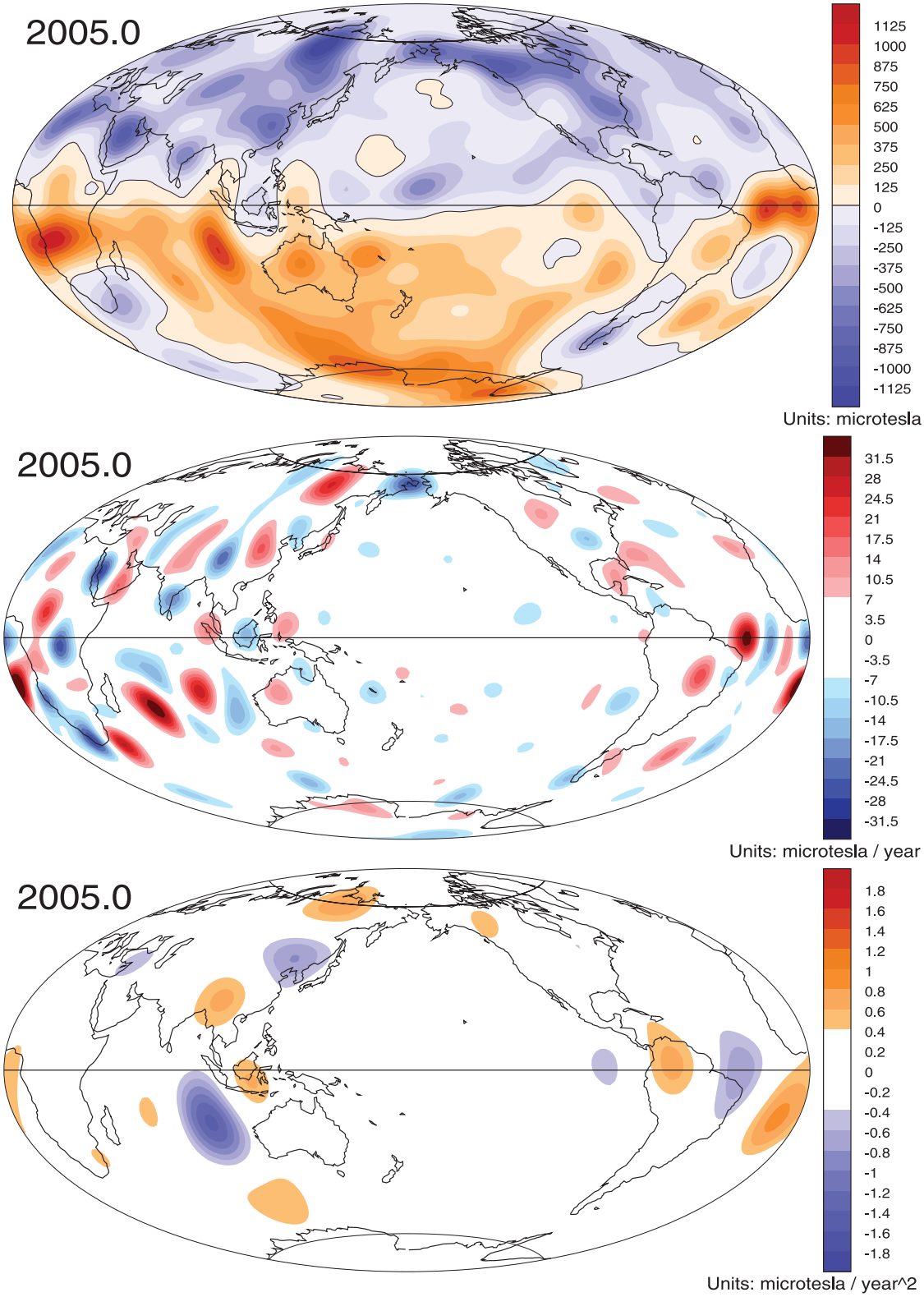

Figure 13. Maps of the radial MF, SV and SA from *gufm-sat-E3* in 2005 at the core surface, centred on the Pacific hemisphere. Hammer–Aitoff projection is used; the tangent cylinder and the geographic equator are marked.

the core surface. Model *gufm-sat-E3*, constructed using entropy regularization in space, possesses a MF spectral slope that decays at an approximately constant rate out to degree 24. All the *gufm-sat* models possess a very similar global misfit to the observations and adequately explain annual differences of processed observatory monthly means.

Our models show that rapid field evolution has taken place in the past decade under the Cocos Islands, associated with the

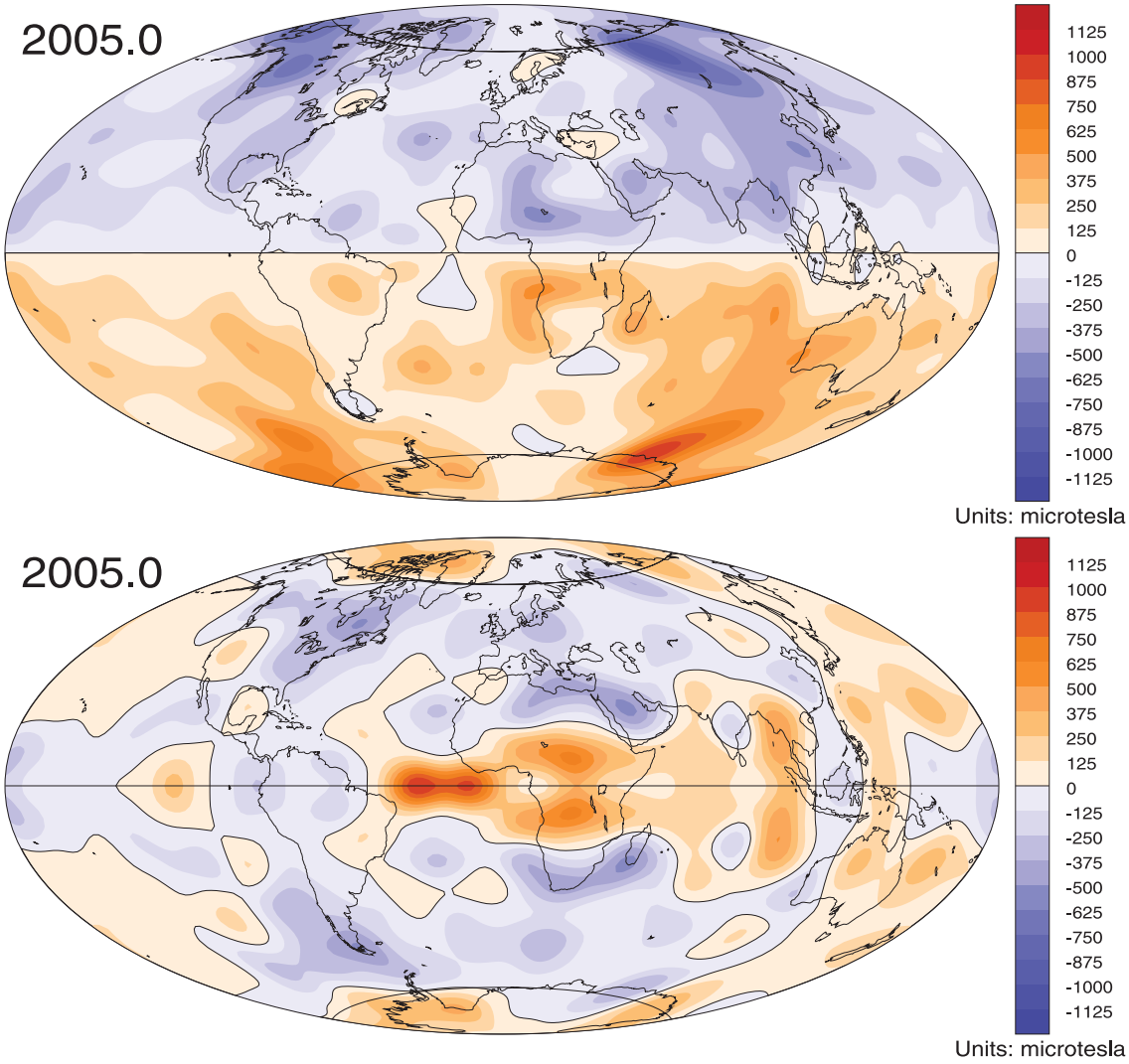

Figure 14. Decomposition of radial field at core surface in 2005.0 from *gufm-sat-E3*, into its equatorially antisymmetric component (top panel) and its equatorially symmetric component (bottom panel). Hammer–Aitoff projection is used; the tangent cylinder and the geographic equator are marked by solid black lines.

continuing growth of a strong normal flux patch. This patch appears to be the newest member of the series of intense westward moving field concentrations at low latitudes south of the geomagnetic equator, and we find it has already begun to move westwards. The westward motion of field features north and south of the magnetic equator under the Atlantic hemisphere dominates the morphology of SV and SA at the core surface over the past 10 yr. Producing accurate, dynamically consistent, models of this process will be essential for future improvements in operational predictions of geomagnetic field evolution. Axial dipole decay has continued over the past 10 yr and we find it is primarily due to changes in the magnetic field in the southern hemisphere. These changes include both the northward transport of normal flux in the eastern Indian Ocean as well as the continued intensification and southward movement of the reversed flux features under South Africa and South America, but also a number of less easily classified small scale changes in field morphology. Both SV and SA are found to be much weaker in the Pacific hemisphere where MF amplitudes are also lower. The present field is found to contain significant energy in both the equatorially symmetric and antisymmetric components, with strong concentrations of equatorially symmetric energy prominent at low latitudes.

This study has highlighted a number of modelling issues that require further investigation. First, how best to separate the core field from the crustal field remains a fundamental and problematic issue. The traditional approaches have been either to choose a spherical harmonic truncation level, or as we have done here to penalize norms of spatial complexity at the core surface in the hope of excluding crustal effects. Neither approach is completely satisfactory, and it is likely that some traces of the crustal field remains in all current models of the core field. Perhaps joint inversions for the core and crustal field using stronger prior knowledge on each source may enable some progress, but appropriately formulating such *a priori* information is challenging. Another concern is that the strong temporal smoothing applied in our models, and those of other workers, may filter out the signatures of interesting short timescale core dynamics. Efforts to move beyond standard temporal regularization norms and towards more physically motivated temporal prior information are

now necessary. The determination of both the very large (degree 1) and small scale (above spherical harmonic degree 9) of SA remains troublesome, with the results depending strongly on the temporal endpoint conditions applied—the constraints from observations on such scales are not sufficiently strong to completely outweigh the influence of the modelling choices. Further high quality satellite data are anticipated in the next few years from the upcoming ESA *Swarm* mission (Friis-Christensen *et al.* 2006) which should permit improved internal–external field separation, and hence hopefully better constraints on the core field acceleration. The lack of reliable uncertainty estimates for core surface field models is in part an unfortunate consequence of *ad hoc* regularization or model truncation; here we have presented three models in an attempt to illustrate the flexibility available when producing models that are compatible with the observations. Finally, a timespan of 10 yr is unfortunately too short to provide observational tests of many aspects of core dynamics that can currently be modelled. In a future study, we will use the satellite data sets described here, and a similar modelling approach, in an update of the *gufm1* historical field model that will extend to 2010.

7 ACKNOWLEDGMENTS

We thank the institutes responsible for supporting the CHAMP, Ørsted and SAC-C missions for operating the satellites and making the data available. We also thank the national institutes that support ground magnetic observatories and INTERMAGNET for promoting high standards of practise. Contour maps were produced using the 'magmap' and 'color' software packages developed by R. L. Parker. David Gubbins and Vincent Lesur are thanked for their insightful reviews that helped to improve the manuscript. The GEOSPACE consortium (NERC, UK) is thanked for helpful discussions and support for workshops. The International Space Science Institute is acknowledged for its support of international team no. 176. CF was partially supported by NERC grant NER/O/S/2003/0064. This work was also supported by the Centre National d'Etudes Spatiales (CNES) for the preparation of the Swarm mission.

REFERENCES

Amit, H. & Christensen, U., 2008. Accounting for magnetic diffusion in core flow inversions from geomagnetic secular variation, *Geophys. J. Int.,* **175,** 913–924.

Amit, H. & Olson, P., 2006. Time–average and time–dependent parts of core flows, *Phys. Earth planet. Int.,* **155,** 120–139.

Aster, R., Borchers, B. & Thurber, C., 2005. *Parameter Estimation and Inverse Problems,* Elsevier, Amsterdam.

Aubert, J., Amit, H. & Hulot, G., 2007. Detecting thermal boundary control in surface flows from numerical dynamos, *Phys. Earth planet. Int.,* **160,** 143–156.

Bloxham, J., 1992. The steady part of the secular variation of the Earth's magnetic field, *J. geophys. Res.,* **97**(B13), 19 565–19 579.

Bloxham, J. & Gubbins, D., 1985. The secular variation of Earth's magnetic field, *Nature,* **317,** 777–781.

Bloxham, J. & Jackson, A., 1992. Time-dependent mapping of the magnetic field at the core-mantle boundary, *J. geophys. Res.*, **97**(B13), 19 537–19 563.

Bloxham, J., Gubbins, D. & Jackson, A., 1989. Geomagnetic secular variation, *Phil. Trans. R. Soc. Lond. A.,* **329,** 415–502.

Bullard, E.C., Freedman, C., Gellman, H. & Nixon, J., 1950. The westward drift of the Earth's magnetic field, *Phil. Trans. R. Soc. Lond. A.,* **243,** 67–92.

Christensen, U.R. & Olson, P., 2003. Secular variation in numerical geodynamo models with lateral variations of boundary heat flow, *Phys. Earth planet. Inter.,* **138,** 39–54.

Chulliat, A., Thébault, E., Hulot, G., 2010. Core field acceleration pulse as a common cause of the 2003 and 2007 geomagnetic jerks, *Geophys. Res. Lett.,* **37,** doi:10.1029/2009GL042019.

Claerbout, J. & Muir, F., 1973. Robust modelling with erratic data, *Geophysics,* **38,** 826–844.

Constable, C.G., 1988. Parameter estimation in non-Gaussian noise, *Geophys. J.,* **94,** 131–142.

De Boor, C., 2001. *A Practical Guide to Splines,* Springer, New York, NY.

Doell, R.R. & Cox, A., 1971. Pacific geomagnetic secular variation, *Science,* **171,** 248–254.

Dumberry, M. & Bloxham, J., 2006. Azimuthal flows in the Earth's core and changes in length of day at millennial timescales, *Geophys. J. Int.,* **165,** 32–46.

Farquharson, C.G. & Oldenburg, D.W., 1998. Non-linear inversion using general measures of data misfit and model structure. *Geophys. J. Int.,* **134,** 213–227.

Finlay, C.C. & Jackson, A., 2003. Equatorially dominated magnetic field change at the surface of Earth's core, *Science,* **300,** 2084–2086.

Finlay, C.C., Dumberry, M., Chulliat, A. & Pais, A.M., 2010. Short timescale core dynamics: theory and observations, *Space Sci. Rev.,* **155,** 177–218.

Fisk, H.W., 1931. Isopors and isoporic movements. *Internat. Geodetic Geophys. Union, Section Terrest. Magnet. Elec. Bull. Stockholm,* **8,** 280–292.

Fournier, A. *et al.*, 2010. An introduction to geomagnetic data assimilation and predictability in geomagnetism, *Space Sci. Rev.,* **155,** 247–291.

Fournier, A., Aubert, J. & Thébault, E., 2011. Inference on core surface flow from observations and 3-D dynamo modelling, *Geophys. J. Int.,* **186,** 118–136.

Friis-Christensen, E., Lühr, H. & Hulot, G., 2006. Swarm: a constellation to study the Earth's magnetic field, *Earth Planets Space,* **58,** 351–358.

Gillet, N., Jackson, A. & Finlay, C.C., 2007. Maximum entropy regularization of time-dependent geomagnetic field models, *Geophys. J. Int.,* **171,** 1005–1016.

Gillet, N., Pais, M.A. & Jault, D., 2009. Ensemble inversion of time-dependent core flow models, *Geophys. Geochem. Geosyst.,* **10,** doi:10.1029/2008GC002290.

Gillet, N., Lesur, V. & Olsen, N., 2010. Geomagnetic core field secular variation models, *Space Sci. Rev.,* **155,** 129–145.

Gillet, N., Schaeffer, N. & Jault, D., 2011. Rationale and geophysical evidence for quasi-geostrophic rapid dynamics within the Earth's outer core, *Phys. Earth planet. Int.,* **187,** 380–390.

Green, P.J. & Silverman, B.W., 1994. *Nonparametric Regression and Generalized Linear Models: A Roughness Penalty Approach*. Chapman and Hall, London.

Gubbins, D., 1983. Geomagnetic field analysis - I. Stochastic inversion, *Geophys. J. R. astr. Soc.,* **73,** 641–652.

Gubbins, D., 1987. Mechanism for geomagnetic polarity reversals, *Nature,* **326,** 167–169.

Gubbins, D., 1996. A formalism for the inversion of geomagnetic data for core motions with diffusion, *Phys. Earth. planet. Int.,* **98,** 193–206.

Gubbins, D., 2004. *Time Series Analysis and Inverse Theory for Geophysicists,* Cambridge University Press, Cambridge.

Gubbins, D. & Roberts, N., 1983. Use of the frozen flux approximation in the interpretation of archeomagnetic and paleomagnetic data, *Geophys. J. R. astr. Soc.,* **73,** 675–687.

Gubbins, D. & Bloxham, J., 1985. Geomagnetic field analysis - III. Magnetic fields on the core-mantle boundary, *Geophys. J. R. astr. Soc.,* **80,** 695–713.

Gubbins, D. & Bloxham, J., 1987. Morphology of the geomagnetic field and implications for the geodynamo, *Nature,* **325,** 509–511.

Gubbins, D. & Gibbons, S., 2004. Low Pacific Secular Variation, *Timescales of the Paleomagnetic field, Geophysical Monograph Series,* **145,** 279–286.

Gubbins, D. & Kelly, P., 1993. Persistent patterns in the geomagnetic field over the past 2.5 myr, *Nature,* **365,** 829–832.

Gubbins, D. & Zhang, K., 1993. Symmetry properties of the dynamo equations for paleomagnetism and geomagnetism, *Phys. Earth planet. Int.,* **75,** 225–241.

Gubbins, D., Jones, A.L. & Finlay, C.C., 2006. Fall in Earth's magnetic field is erratic, *Science,* **321,** 900–903.

Gull, S., Daniell, G., 1978. Image reconstruction from incomplete and noisy data, *Nature,* **272,** 686–690.

Gull, S. & Skilling, J., 1984. Maximum entropy method in image processing, *IEE Proc.,* **131,** 646–659.

Gull, S. & Skilling, J., 1990. *The MEMSYS5 User's Manual*. Maximum Entropy Data Consultants Ltd., Royston.

Hamilton, B., Macmillan, S. & Thomson, A., 2010. The BGS magnetic field candidate models for the 11th generation IGRF, *Earth Planets Space,* **62,** 737–744.

Hide, R., 1967. Motions of the Earth's core and mantle and variations in the main geomagnetic field, *Science,* **157,** 55–56.

Hogg, R.V., 1979. Statistical robustness: one view of its use in applications today, *Am. Stat.,* **33,** 717–730.

Holme, R., 2000. Modelling of attitude error in vector magnetic data: application to Ørsted data, *Earth Planets Space,* **52,** 1187–1197.

Holme, R., 2007. Large–scale Flow in the Core, in *Treatise on Geophysics,* Vol. 8, Chapter 8.04, pp. 107–130, ed. Olson, P., Elsevier, Amsterdam.

Holme, R. & Bloxham, J., 1995. Alleviation of Backus effect in geomagnetic field modelling, *Geophys. Res. Lett.,* **22,** 1641–1644.

Holme, R. & Olsen, N., 2006. Core surface flow modelling from high-resolution secular variation, *Geophys. J. Int.,* **166,** 518–528.

Holme, R., Olsen, N. & Bairstow, F.L., 2011. Mapping geomagnetic secular variation at the core-mantle boundary, *Geophys. J. Int.,* **186,** 521–528.

Huber, P.J., 1996. Robust Statistical Procedures. SIAM.

Hulot, G., Eymin, C., Langlais, B. & Mandea, M., 2002. Small-scale structure of the geodynamo inferred from Ørsted and Magsat satellite data, *Nature,* **416,** 620–623.

Hulot, G., Olsen, N. & Sabaka, T.J., 2007. The present field, in *Treatise on Geophysics,* Vol. 5, Geomagnetism, pp. 33–75, ed. Kono, M., Elsevier, Amsterdam.

Jackson, A., 1997. Time-dependency of tangentially geostrophic core surface motions, *Phys. Earth planet. Inter.,* **103,** 293–311.

Jackson, A., 2003. Intense equatorial flux spots on the surface of Earth's core, *Nature,* **464,** 760–763.

Jackson, A., Jonkers, A.R.T. & Walker, M.R., 2000. Four centuries of geomagnetic secular variation from historical records, *Phil. Trans. R. Soc. Lond. A.,* **358,** 957–990.

Jackson, A., Constable, C. & Gillet, N., 2007. Maximum entropy regularization of the geomagnetic core field inverse problem, *Geophys. J. Int.,* **171,** 995–1004.

Kuang, W. & Bloxham, J., 1998. Numerical dynamo modelling: comparison with the Earth's magnetic field, in *The Core-Mantle Boundary Region,* Geodynamics Series Vol. 28, pp. 197–209, American Geophysical Union, Washington DC.

Kuvshinov, A. & Olsen, N., 2006. A global model of mantle conductivity derived from 5 years of CHAMP, Ørsted, and SAC-C magnetic data, *Geophys. Res. Lett.,* **33,** doi:10.1029/2006GL027083.

Lesur, V., Wardinski, I., Rother, M. & Mandea, M., 2008. GRIMM: the GFZ reference internal magnetic model based on vector satellite and observatory data, *Geophys. J. Int.,* **173,** 382–394.

Lesur, V., Wardinski, I., Hamoudi, M. & Rother, M., 2010. The second generation of the GFZ Reference Internal magnetic Model: GRIMM-2, *Earth, Planets, Space,* **62,** 765–773.

Lowes, F.J., 1974. Spatial power spectrum of the main geomagnetic field, *Geophys. J. R. astr. Soc.,* **36,** 717–730.

Luenberger, D.G., 1969. *Optimization by Vector Space Methods,* John Wiley & Sons, New York, NY.

Maus, S., Rother, M., Stolle, C., Mai, W., Choi, S., Lühr, H., Cook, D. & Roth, C., 2006. Third generation of the Potsdam Magnetic Model of the Earth (POMME), *Geophys. Geochem. Geosyst.,* **7,** Q07008, doi:10.1029/2006GC001269.

Maus, S., Manoj, C., Rauberg, J., Michaelis, I. & Lühr, H., 2010. NOAA/NGDC candidate models for the 11th generation International Geomagnetic Reference Field and the concurrent release of the 6th generation POMME magnetic model, *Earth Planets Space,* **62,** 729–735.

Mayaud, P.N., 1980. *Derivation, Meaning and Use of Geomagnetic Indices,* AGU, Washington.

Medin, A.E., Parker, R. & Constable, S., 2007. Making sound inferences from geomagnetic sounding, *Phys. Earth planet. Int.,* **160,** 51–59.

Olsen, N., 2002. A model of the geomagnetic field and its secular variation for epoch 2000 estimated from Ørsted data, *Geophys. J. Int.,* **149,** 454–462.

Olson, P. & Amit, H., 2006. Changes in Earth's dipole, *Naturwissenschaften,* **93,** 519–542.

Olson, P. & Christensen, U.R., 2002. The time-averaged magnetic field in numerical dynamos with non-uniform boundary heat flow, *Geophys. J. Int.,* **151,** 809–823.

Olsen, N. & Mandea, M., 2007. Investigation of a secular variation impulse using satellite data: the 2003 geomagnetic jerk, *Earth planet. Sci. Lett.,* **255,** 94–105.

Olsen, N. & Mandea, M., 2008. Rapidly changing flows in the Earth's core, *Nat. Geosci.,* **1,** 390–394.

Olsen, N., Lühr, H., Sabaka, T.J., Mandea, M., Rother, M., Tøffner-Clausen, L. & Choi, S., 2006. CHAOS- a model of the Earth's magnetic field derived from CHAMP, Ørsted and SAC-C magnetic satellite data, *Geophys. J. Int.,* **166,** 67–75.

Olsen, N., Mandea, M., Sabaka, T. & Tøffner-Clausen, L., 2009. CHAOS-2-a geomagnetic field model derived from one decade of continuous satellite data, *Geophys. J. Int.,* **179,** 1477–1487.

Olsen, N., Mandea, M., Sabaka, T.J. & Tøffner-Clausen, L., 2010. The CHAOS-3 geomagnetic field model and candidates for the 11th generation IGRF, *Earth Planets Space,* **62,** 719–727.

Pais, M.A. & Jault, D., 2008. Quasi-geostrophic flows responsible for the secular variation of the Earth's magnetic field, *Geophys. J. Int.,* **173,** 421–443.

Parker, R.L., 1994. *Geophysical Inverse Theory,* Princeton University Press, Princeton, NJ.

Sabaka, T.J., Olsen, N. & Purucker, M.E., 2004. Extending comprehensive models of the Earth's magnetic field with Oersted and CHAMP data, *Geophys. J. Int.,* **159,** 521–547.

Sakuraba, A. & Roberts, P., 2009. Generation of a strong magnetic field using uniform heat flux at the surface of the core, *Nat. Geosci.,* **2,** 802–805.

Schlossmacher, E.J., 1971. An iterative technique for absolute deviations curve fitting, *J. Am. Stat. Assoc.,* **68,** 857–865.

Shure, L., Parker, R. & Backus, G., 1982. Harmonic splines for geomagnetic modelling, *Phys. Earth planet. Inter.,* **28**(3), 215–229.

Sivia, D. & Skilling, J., 2006. *Data Analysis: A Bayesian Tutorial*, Oxford University Press, Oxford.

Sreenivasan, B. & Gubbins, D., 2008. Dynamos with weakly convecting outer layers: implications for core-mantle boundary interaction, *Geophys. Astrophys. Fluid Dyn.,* **102,** 395–407.

Stockmann, R., Finlay, C.C. & Jackson, A., 2009. Imaging Earth's crustal magnetic field with satellite data: a regularized spherical triangle tessellation approach, *Geophys. J. Int.,* **179,** 929–944.

Tarantola, A., 2005. *Inverse Problem Theory and Methods for Model Parameter Estimation*. SIAM, Society for Industrial and Applied Mathematics, Philadelphia.

Thébault, E., Hemant, K., Hulot, G. & Olsen, N., 2009. On the geographical distribution of induced time-varying crustal magnetic fields, *Geophys. Res. Lett.,* **36,** doi:10.1029/2008GL036416.

Thébault, E., Chulliat, A., Maus, S., Hulot, G., Langlais, B., Chambodut, A. & Menvielle, M., 2010. IGRF candidate models at times of rapid changes in core field acceleration, *Earth Planets Space,* **62,** 753–764.

Thomson, A. & Lesur, V., 2007. An improved geomagnetic data selection algorithm for global geomagnetic field modelling, *Geophys. J. Int.,* **169,** 951–963.

Velímský, 2010. Electrical conductivity in the lower mantle: constraints from CHAMP satellite data by time-domain EM induction modelling, *Phys. Earth planet. Int.,* **180,** 111–117.

Walker, A.D. & Backus, G.E., 1996. On the difference between the average values of B_r^2 in the atlantic and pacific hemipheres, *Geophys. Res. Lett.,* **23,** 1965–1968.

Walker, M.R. & Jackson, A., 2000. Robust modelling of the Earth's magnetic field, *Geophys. J. Int.,* **143,** 799–808.

Wardinski, I., Holme, R., 2006. A time-dependent model of the Earth's magnetic field and its secular variation for the period 1980-2000. *J. geophys. Res.,* **111,** doi:10.1029/2006JB004401.

Wardinski, I. & Holme, R., 2011. Signal from noise in geomagnetic field modelling: denoising data for secular variation studies, *Geophys. J. Int.,* **185,** 653–662.

Wardinski, I. & Lesur, V., 2012. An extended version of the C^3FM geomagnetic field model: application of a continuous frozen-flux constraint, *Geophys. J. Int.,* in press, doi:10.1111/j.1365-246X.2012.05384.x.

Whaler, K. & Gubbins, D., 1981. Spherical harmonic analysis of the geomagnetic field: an example of a linear inverse problem, *Geophys. J. R. Soc. Lond.,* **65,** 645–693.